In Search of the Kitaev Interactions in Low-Dimensional Yttrium-Doped Calcium Iridates

IN SEARCH OF THE KITAEV INTERACTIONS IN LOW-DIMENSIONAL YTTRIUM-DOPED CALCIUM IRIDATES: $\mathrm{CA}_{5-X}\mathrm{Y}_X\mathrm{IR}_3\mathrm{O}_{12}$

By

YIJIA ZI, H.B.Sc.

A Thesis Submitted to the School of Graduate Studies
in the Partial Fulfillment of the Requirements for the Degree of Master of Science

McMaster University November 22, 2023

McMaster University
Master of Science (2023)
Hamilton, Ontario (Physics and Astronomy)

TITLE: In Search of the Kitaev Interactions in Low-Dimensional Yttrium-Doped Calcium Iridates: $Ca_{5-x}Y_xIr_3O_{12}$
AUTHOR: Yijia Zi, H.B.Sc. (University of Toronto)
SUPERVISOR: Dr. J. P. Clancy
NUMBER OF PAGES: xiii, 71

Abstract

The goal of this thesis is to search a potential experimental realization of the low-dimensional Kitaev chain in calcium iridates, satisfying the two criteria proposed by G. Jackeli and G. Khaliullin. These criteria state the necessity for a material with a ground state characterized by $J_{\text{eff}} = 1/2$ and a 90° metal-oxygen-metal (TM-O-TM) bond geometry to facilitate the emergence of bond-dependent Kitaev interactions. Our initial potential candidate, Ca_2IrO_4, could not be synthesized under any attempted conditions. Structural and magnetic analyses revealed an antiferromagnetic transition consistent with $Ca_5Ir_3O_{12}$, a calcium-deficient version of Ca_2IrO_4, with a mixed valence state of $Ir^{4.67+}$. This deviation from the ideal pure Ir^{4+} valence state hindered the realization of a pure Kitaev chain. We then proposed the second potential candidate, $Ca_{5-x}Y_xIr_3O_{12}$. By introducing $x = 2$ (i.e. 40%) yttrium doping, the valence of $Ca_5Ir_3O_{12}$ can be tuned from $Ir^{4.67+}$ to Ir^{4+}. The highest achieved doping level, $x = 1.52(2)$, resulted in an $Ir^{4.16+}$ oxidation state, very close to the desired pure Ir^{4+} chain. Further structural analysis revealed deviations from the ideal TM-O-TM bond angles necessary for realizing pure Kitaev interactions. Regardless, $Ca_{5-x}Y_xIr_3O_{12}$ samples exhibit intriguing properties. First, the achieved doping levels exceed those in previously studied doped $Ca_5Ir_3O_{12}$. Second, electronic characterizations reveal consistency with a spin-orbit-driven state in all synthesized $Ca_{5-x}Y_xIr_3O_{12}$ samples. Third, magnetic susceptibility data demonstrate that as the doping level increases to the range of 5-20%, the magnetic transition observed in the parent compound at around 7K completely vanishes. With further doping to 25-30%, a new magnetic transition emerges at around 11-13K. This research opens up additional avenues for further investigation of $Ca_{5-x}Y_xIr_3O_{12}$, as well as potential candidates for realizing Kitaev interactions.

Acknowledgements

This thesis would not have been possible without the help and support of a long list of individuals. I would like to take this moment to express my gratitude to all those who have been supporting me throughout my Master's journey. First and foremost, I extend my deepest thanks to my supervisor, Dr.Pat Clancy, who provided me with the opportunity to start my research journey in the field of physics. His wisdom, patience, and optimism have been my guiding lights over the past two years. The unique 'character-building experiences' he offered undeniably shaped me into a stronger human being. I am also grateful to my other two supervisory committee members, Dr.Bruce Gaulin and Dr.Graeme Luke, for their invaluable guidance throughout my Master's study. I extend special thanks to Dr.James Britten at the McMaster Analytical X-Ray Diffraction Facility for sharing his expertise in single crystal XRD techniques and for helping me tackle the numerous challenges that arose during the process. Dr.Qiang Chen's guidance with crystal growth and furnace issues, along with Dr.James Beare's assistance in using SQUID, were greatly appreciated. I also want to acknowledge Dr.Chris Pollock from Cornell High Energy Synchrotron Source for his support during our PIPOX experiments. My gratitude extends to my colleagues at McMaster, Monika Azmanska and Daniel Dobrowolski, for their support and extraordinary patience during our experiments. Without their presence, I would not have been able to complete any of the experiments, both mentally and physically. I would like to take a moment to thank my parents, for their 'understanding, love, and encouragement'. A special thanks to my dearest father, Jiquan Zi, for both his financial and mental support, and thanks for his willingness and patience to talk me through my moments of crisis, even in the midnight. Lastly, as I pen down this section on Thanksgiving, in keeping with the festive vibes, I want to extend my thanks to all those whose names might not have found their way into this text but who provided support during these two years of study.

Two pieces of yeast were discussing the possible purposes of life as they ate sugar and suffocated in their own excrement. Because of their limited intelligence, they never came close to guessing that they were making champagne. - Kurt Vonnegut (Breakfast of Champions)

Cheers, my friends.

Contents

List of Figures

List of Tables

Chapter 1

Introduction

5d transition metal iridates are intriguing materials due to their potential for exhibiting a wide variety of exotic electronic and magnetic ground states. The origin of these fascinating properties lies in the complex interplay between crystal electric fields, spin-orbit coupling, and electronic correlations. One particularly interesting phenomenon within these systems is the emergence of bond-dependent Kitaev interactions. Initially, research interest primarily focused on theoretical calculations and the search for experimental realizations of Kitaev interactions on the originally proposed honeycomb lattice. More recently, research has expanded to include other lattice types beyond the conventional honeycomb lattice. This chapter serves as an introduction to the basic theoretical framework necessary for understanding Kitaev interactions. Furthermore, it provides a few examples of Kitaev interactions realized on honeycomb and other lattice types, which helps motivate our search for an experimental realization of Kitaev interactions on quasi-one-dimensional chains.

1.1 5d Transition Metals in the $J_{\text{eff}} = 1/2$ Model

In the realm of electron correlation physics, 3d transition metals have been extensively explored. They are characterized by large Coulomb repulsion and narrow energy bands, providing good experimental realizations for Mott physics based on the Hubbard Hamiltonian. This exploration has led to intriguing phenomena, including metal-insulator transitions, Mott insulators, and high-temperature superconductivity [6, 7, 8].

However, as we delve into the heavy 5d transition metals lower down the periodic table, a shift occurs. These elements are heavier, and their wavefunctions are more spatially extended, resulting in reduced wavefunction overlap and diminished electron correlation effects. Simultaneously, the influence of spin-orbit coupling (proportional to the atomic number to the fourth power) undergoes a dramatic enhancement when transitioning from 3d to 5d transition metals [9]. This sets the stage for a fascinating interplay between electron repulsion (U), arising from the Coulomb interaction between electrons, and spin-orbit coupling (λ), leading to a rich phase diagram as depicted in Figure 1.1.

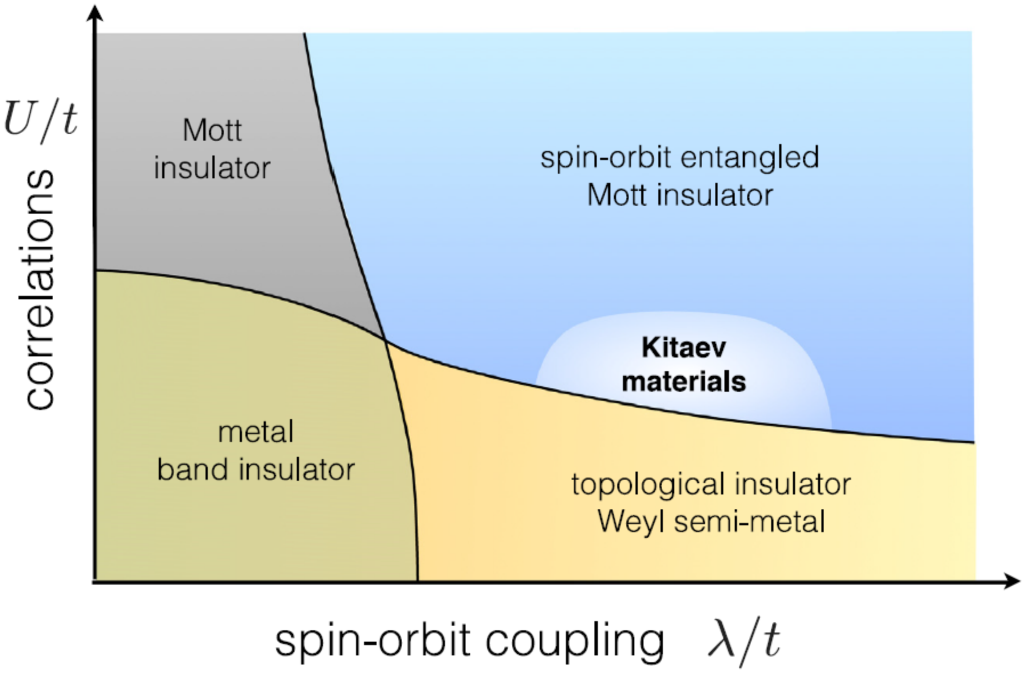

FIGURE 1.1: Phase diagram illustrating the interplay between electron repulsion (U) and spin-orbit coupling (λ). Figure from [1].

Furthermore, when 5d transition metals are placed in an octahedral crystal electric field, intriguing electronic properties emerge. Consider a simple 5d transition ion with five-fold degenerate d-states. When this ion is surrounded by an octahedral ligand cage, the full rotational symmetry of $SU(2)$ is broken, leading to a lower symmetry described by the octahedral symmetry group O_h. As a result, the initial five-fold degenerate d-states split into higher energy two-fold degenerate e_g states and lower energy three-fold degenerate t_{2g} states, as depicted in Figure 1.2. The e_g states correspond to the $d_{x^2-y^2}$ and d_{z^2} orbitals, where the electron orbitals point towards the ligand, resulting in higher Coulomb repulsion energy and thus a higher-energy state. In contrast, the t_{2g} states correspond to the d_{xy}, d_{xz}, and d_{yz} orbitals, where the electron orbitals point away from the ligand, yielding a smaller Coulomb repulsion energy and a lower-energy state.

Unlike in the conventional 5d states with angular momentum $L = 2$, due to substantial crystal field splitting ($10Dq$) between the e_g and t_{2g} states, in most 5d transition metal oxides and halides, electrons preferentially occupy the lower-energy t_{2g} states. This results in an effective angular momentum of $L_{\text{eff}}, = 1$, with three degenerate states formed through superpositions of different d orbitals ($|d_{xy}\rangle, |d_{xz}\rangle, |d_{yz}\rangle$) that point away from the ligand. The three t_{2g} degenerate states are illustrated in Equation 1.1.1 [10].

$$\begin{aligned} |l_z = 0\rangle &= |d_{xy}\rangle \\ |l_z = 1\rangle &= -\frac{1}{\sqrt{2}}(i|d_{xz}\rangle + |d_{yz}\rangle) \\ |l_z = -1\rangle &= -\frac{1}{\sqrt{2}}(i|d_{xz}\rangle - |d_{yz}\rangle) \end{aligned} \tag{1.1.1}$$

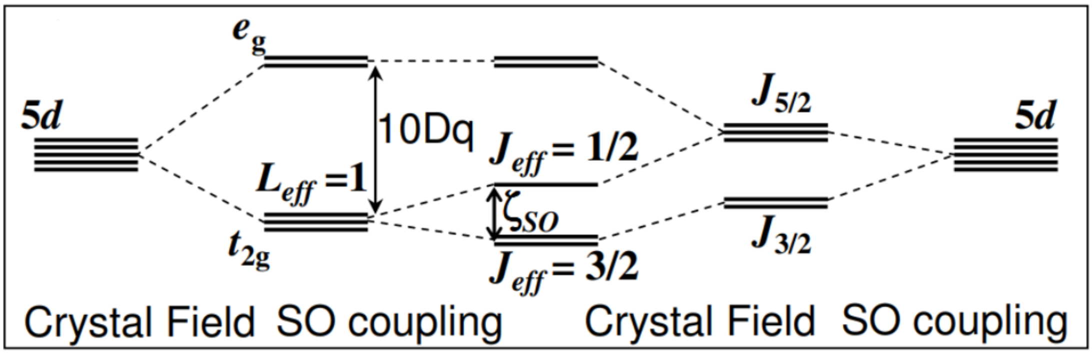

FIGURE 1.2: Schematic representation of the $J_{\text{eff}} = 1/2$ picture proposed by B.J. Kim, et al. Figure from [2].

Now, consider the octahedral crystal electric field in the strong spin-orbit coupling limit by including the spin degree of freedom. As illustrated in Figure 1.2, when transitioning from left to right (applying CEF and then SOC), the initially three-fold degenerate t_{2g} states further split into two states: a two-fold degenerate state with an effective total momentum of $J_{\text{eff}} = 1/2$ and a four-fold degenerate state with $J_{\text{eff}} = 3/2$. The two eigenstates for $J_{\text{eff}} = 1/2$ are superpositions of different orbital states, from Equation 1.1.1, and spin states. These two new states with $J_{\text{eff}} = 1/2$, shown in Equation 1.1.2 [3], are defined as isospins. They can be visualized in Figure 1.3. Notably, the coupling of orbital states with spin states introduces a directional preference for spins, deviating from their free rotational behavior due to the orbital state.

$$\begin{aligned}|J_{\text{eff}} = 1/2, \downarrow\rangle &= \frac{1}{\sqrt{3}}(|d_{yz,\uparrow}\rangle - i|d_{xz,\uparrow}\rangle - |d_{xy,\downarrow}\rangle)\\ |J_{\text{eff}} = 1/2, \uparrow\rangle &= \frac{1}{\sqrt{3}}(|d_{yz,\downarrow}\rangle + i|d_{xz,\downarrow}\rangle + |d_{xy,\uparrow}\rangle)\end{aligned} \tag{1.1.2}$$

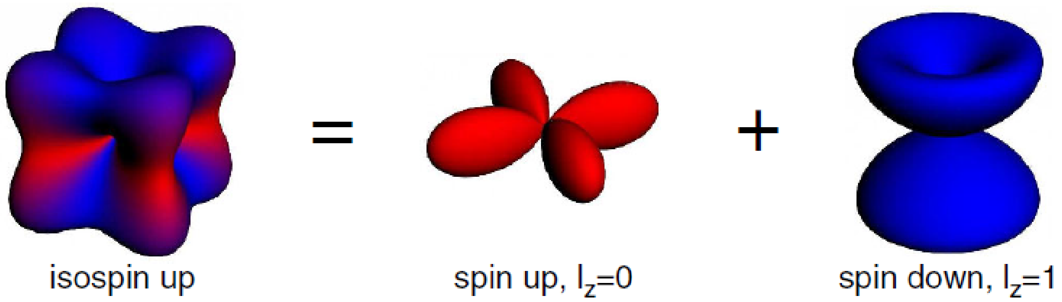

FIGURE 1.3: Visualization of an isospin-up state ($|J_{\text{eff}} = 1/2, \uparrow\rangle$), a superposition of $l_z = 0$ spin-up state and $l_z = 1$ spin-down states. Figure from [3].

The same result occurs when transitioning from right to left in Figure 1.2 (applying SOC and then CEF). In this case, a 5d transition metal with spin-orbit coupling experiences the splitting of its five-fold degenerate state into a three-fold degenerate state with a total momentum of $J = 5/2$ and a two-fold degenerate state with a total momentum of $J = 3/2$. Subsequently, within an octahedral crystal electric field, the three-fold $J = 5/2$ state splits into the upper two-fold degenerate e_g states and the lower $J_{\text{eff}} = 1/2$ state. This explains why the $J_{\text{eff}} = 1/2$ state has a higher energy compared to the $J_{\text{eff}} = 3/2$ state.

The $J_{\text{eff}} = 1/2$ model plays an important role in understanding the electronic and magnetic properties of many 4d and 5d transition metals. In terms of electronic properties, unlike conventional Mott insulators driven by strong electronic correlations, the $J_{\text{eff}} = 1/2$ model provides an alternative mechanism to achieve a Mott insulating state with relatively small electronic correlations. For instance, ions with a d^5 electronic configuration, such as Ru^{3+} with a $4d^5$ valence and Ir^{4+} with a $5d^5$ valence, which are both expected to be metals based on band theory, exhibit insulating behavior in the $J_{\text{eff}} = 1/2$ picture. In this model, the d^5 electronic configuration results in a fully filled $J_{\text{eff}} = 3/2$ band and a half-filled $J_{\text{eff}} = 1/2$ band. As a consequence, even a relatively small Coulomb repulsion can open a Mott gap in the narrow $J_{\text{eff}} = 1/2$ band, leading to the Mott insulator state. This is also referred to as the spin-orbit coupled Mott insulator, which was first experimentally identified in Sr_2IrO_4 [2].

Second, 4d and 5d transition metals exhibit distinct magnetic properties in the strong spin-orbit coupling limit. As shown in Figure 1.4, the spin is reduced with the $J_{\text{eff}} = 1/2$ picture, particularly for the $5d^4$ electronic configuration. In the CEF picture, Ir^{4+} with a $5d^5$ configuration and Ir^{5+} with a $5d^4$ configuration are expected to behave as spin-1/2 and spin-1, respectively. However, when considering the strong spin-orbit coupling limit in the $J_{\text{eff}} = 1/2$ picture, Ir^{4+} with a $5d^5$ configuration and Ir^{5+} with a $5d^4$ configuration are anticipated to behave as spin-1/2 and spin-0, respectively. In this scenario, only Ir^{4+} remains magnetic, while Ir^{5+} becomes non-magnetic.

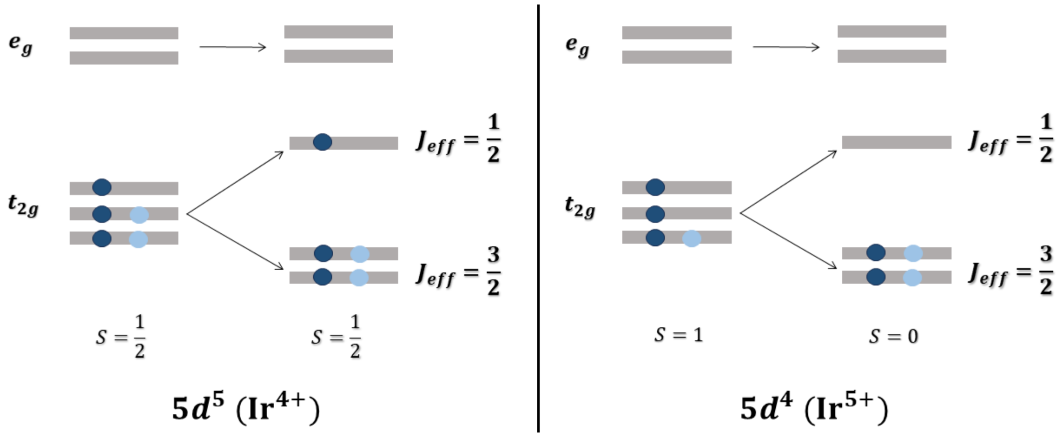

FIGURE 1.4: Electronic configurations of $5d^5$ and $5d^4$ in the CEF and $J_{\text{eff}} = 1/2$ pictures.

1.2 The Kitaev Model and Experimental Realization

In 2006, Alexei Kitaev presented an exact solution for a spin-1/2 system on a two-dimensional honeycomb lattice, for a Hamiltonian with highly anisotropic bond-dependent interactions, resulting in a quantum spin liquid (QSL) ground state, where the formation of long-range magnetic order was prevented by strong quantum fluctuations. QSL are another fascinating research topic due to their intriguing properties, including long-range entanglement between spins and fractional spin excitations. These properties hold the potential for applications in quantum communication and quantum computation. Initially, QSL states were only realized through geometric frustration, such as in triangular or kagome lattices. Then, Kitaev's model provided a different mechanism to realize QSL states. In Kitaev's quantum spin model on the honeycomb lattice, with no geometric frustration, the magnetic interactions cannot be simultaneously minimized due to the bond-dependent interaction. This results in exchange frustration, which induces strong quantum fluctuations resulting in a Kitaev QSL state [11].

The Kitaev model is illustrated in Figure 1.5. Here, the three types of bonds are labeled as x, y, and z, each describing a different interaction strength. The Hamiltonian is shown in Equation 1.2.1, where $J_{x,y,z}$ represents nearest-neighbor Ising-type spin (σ) interactions along the x, y, and z bonds. This bond-dependent interaction is also known as the Kitaev interaction [4].

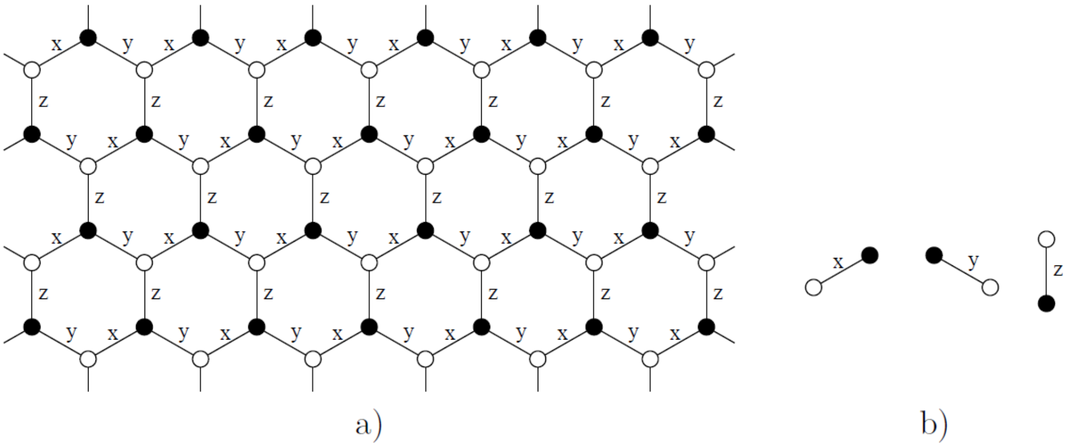

FIGURE 1.5: (a) The Kitaev honeycomb lattice. (b) Three types of bonds labeled as x, y, and z, each with a different interaction strength. Figure from [4].

$$H = -J_x \sum_{x\text{-bonds}} \sigma_i^x \sigma_j^x - J_y \sum_{y\text{-bonds}} \sigma_i^y \sigma_j^y - J_z \sum_{z\text{-bonds}} \sigma_i^z \sigma_j^z \tag{1.2.1}$$

In 2009, G. Jackeli and G. Khaliullin proposed a mechanism for realizing Kitaev interactions in real materials [3]. They emphasized two critical conditions for achieving this goal.

First, they highlighted the importance of strong spin-orbit coupling. To introduce directional magnetic interactions and break the full rotational symmetry (SU(2)) of free spins, one must consider the entanglement of spin and orbital degrees of freedom. This coupling of spin and orbital breaks the SU(2) symmetry in conventional spins, leading to spins with directional dependence. This setup can be achieved by placing a transition metal ion in an octahedral ligand cage, as described in the $J_{\text{eff}} = 1/2$ model discussed earlier. In this context, instead of conventional spins, isospins are considered.

Secondly, they explained the significance of the metal-oxygen-metal (TM-O-TM) bond geometry, as shown in Figure 1.6. The transition metals interact with each other through superexchange interactions via oxygen. In the case of a 180-degree bond formed within corner-sharing octahedra, the dominant interaction is a conventional Heisenberg interaction. In this bond geometry, the nearest-neighbor superexchange hopping matrix is diagonal, and in a given direction, hopping only occurs through the same type of orbitals, as illustrated in Figure 1.6(a) for the x-bond. In this scenario, the exchange Hamiltonian for isospins, as shown in Equation 1.2.2, takes the form of an isotropic Heisenberg interaction, with an additional pseudodipolar interaction term. Surprisingly, under this bond geometry and in the limit of strong spin-orbit coupling, the magnetic interaction closely resembles the Heisenberg interaction observed in cases with weaker spin-orbit coupling. Furthermore, the pseudodipolar interaction term arises from Hund's coupling, deviating from the conventional case where it originates from spin-orbit coupling.

$$H_{ij} = \underbrace{J_1 \vec{S}_i \cdot \vec{S}_j}_{\text{Heisenberg}} + \underbrace{J_2 (\vec{S}_i \cdot \vec{r}_{ij})(\vec{r}_{ij} \cdot \vec{S}_i)}_{\text{pseudodipolar}} \tag{1.2.2}$$

In contrast, for a 90-degree bond formed within edge-sharing octahedra, the isotropic Heisenberg interaction completely vanishes. In this bond geometry, the nearest-neighbor superexchange hopping matrix is only off-diagonal, and hopping only occurs between different types of orbitals within a given bond. The transfer amplitudes for the two possible paths, from the metal to the upper and lower oxygen sites to the other metal site (as shown in Figure 1.6 (b)), interfere destructively. As a result, they cancel out the Heisenberg interaction, giving rise to bond-dependent anisotropic interactions. The Hamiltonian for isospins $S_{i,j}$ linked by the $\gamma = x, y, z$ bond in this scenario is equivalent to the Kitaev interaction, as shown in Equation 1.2.3. Therefore, transition metal ions within edge-sharing octahedra with 90-degree bond geometry offer a promising avenue for realizing the Kitaev interaction in physical materials.

$$H_{ij}^{\gamma} = J S_i^{\gamma} S_j^{\gamma} \tag{1.2.3}$$

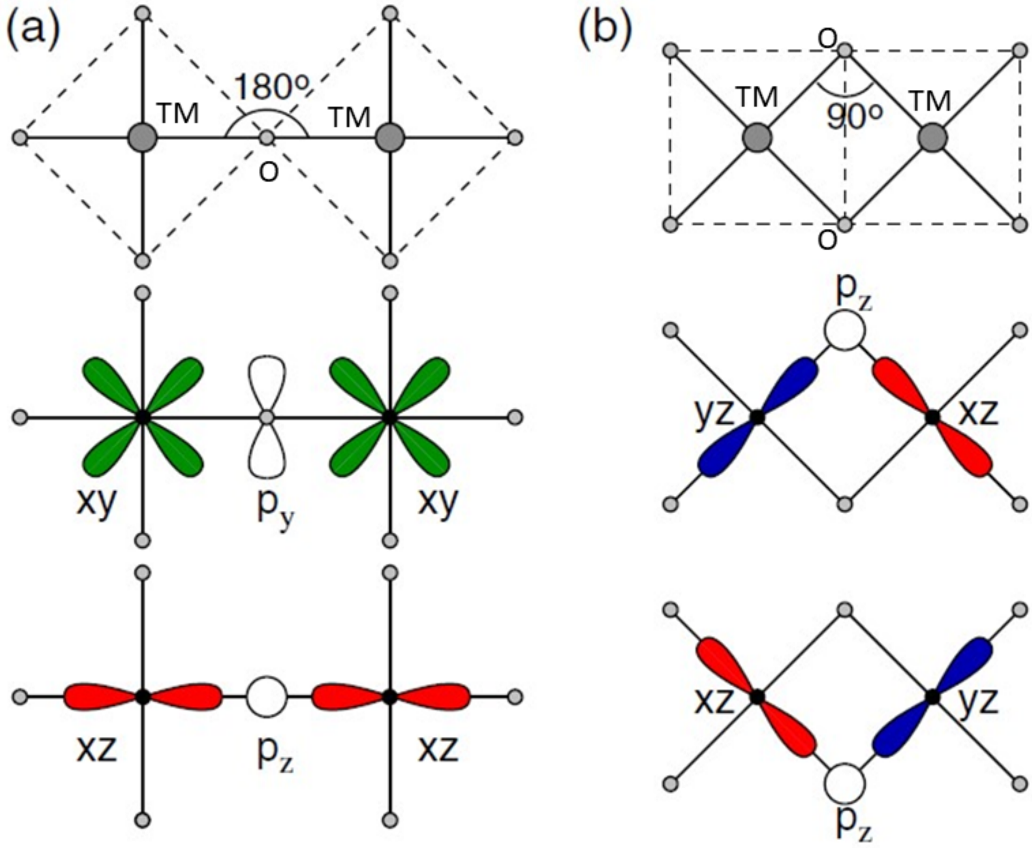

FIGURE 1.6: Two TM-O-TM bond geometries with active orbitals: (a) 180-degree bond geometry as in corner-sharing crystal structures and (b) 90-degree bond geometry as in edge-sharing crystal structures. Figure from [3].

1.3 Possible Candidates for the Kitaev Model

In the search for physical realizations of the Kitaev interaction, one approach is to identify compounds with a 90-degree bond geometry, involving edge-sharing octahedra containing transition metals arranged on a honeycomb lattice, as described in the Kitaev model. G. Jackeli and G. Khaliullin suggested potential candidates in compounds with the A_2BO_3 structure, where 'A' represents an alkali ion and 'B' can be Ir^{4+} or Ru^{3+}

ions known for their strong spin-orbit coupling characteristics [3].

In subsequent experimental studies, many quasi-two-dimensional materials with honeycomb lattice structures were proposed as potential candidates for the Kitaev model. A few representatives include Na_2IrO_3, α-$RuCl_3$, α-Li_2IrO_3, and $H_3LiIr_2O_6$. However, subsequent experimental investigations have shown that, with the exception of $H_3LiIr_2O_6$[12], all other proposed candidates exhibit evidence of long-range magnetic order rather than the desired quantum spin liquid (QSL) state. For instance, Na_2IrO_3 [13] and α-$RuCl_3$ [14] display a zigzag antiferromagnetic ground state, while α-Li_2IrO_3 [15] exhibits a magnetic ground state with incommensurate spiral ordering along the zigzag chains. Although, further inelastic neutron scattering experiments on α-$RuCl_3$ [16] have shown that with a sufficiently large magnetic field, magnetic order is suppressed, potentially leads to a magnetic field-induced QSL phase. These experimental results highlight the challenges of realizing pure Kitaev interactions in real materials under ambient conditions.

One of the complicating factors is the distortion of the octahedral cage, introducing trigonal distortions and deviations from the ideal 90-degree bond geometry. As a result, this reduces the Kitaev interaction and enhances other types of interactions, including non-negligible interactions beyond nearest neighbors [17]. A generic Hamiltonian describing these interactions is shown in Equation 1.3.1, comprising the isotropic Heisenberg interaction with coupling strength J, the Kitaev interaction coupling the γ component of isospins along the γ bond with coupling strength K, and a symmetric off-diagonal Gamma interaction coupling the α and β orthogonal components of isospins along the γ bond with coupling strength Γ [18].

$$H = \sum_{<ij>\in\gamma \text{ bond}} [\underbrace{J\vec{S}_i \cdot \vec{S}_j}_{\text{Heisenberg}} + \underbrace{KS_i^\gamma S_j^\gamma}_{\text{Kitaev}} + \underbrace{\Gamma(S_i^\alpha S_j^\beta + S_i^\beta S_j^\alpha)]}_{\text{Gamma}} \tag{1.3.1}$$

These experimental complications can move the material away from the idealized Kitaev interaction regime. For example, further experimental studies using inelastic neutron scattering and resonant inelastic X-ray scattering along with calculations on the electronic band structure of Li_2IrO_3 [15][19] and Na_2IrO_3[20][21] [22] have revealed the presence of interactions other than Kitaev, such as Heisenberg and Gamma interactions. Additionally, non-negligible interactions with more distant neighbors and structural distortions, including trigonal distortions, must be considered.

Further, theoretical investigations by I. Kimchi and A. Vishwanath in 2014 explored the ground state phase diagram with competing Kitaev-Heisenberg interactions in iridates on various lattice structures. These structures included triangular, hyperkagome, kagome, fcc, and pyrochlore lattices. Except for the triangular and fcc lattices, the other lattices showed a non-spin-ordered quantum phase with extensive degeneracy in their respective phase diagrams [23]. This research opened up the possibility of realizing Kitaev interactions beyond the honeycomb lattice. For instance, $NaRuO_2$ (triangular lattice)[24] and some double perovskites such as La_2MgIrO_6 and La_2ZnIrO_6 (fcc lattice)[25] were experimentally shown to host Kitaev interactions.

Moreover, theoretical studies have revealed that the Kitaev-Heisenberg honeycomb-lattice model can be understood in terms of coupled one-dimensional Kitaev-Heisenberg chains [5]. This insight has sparked interest in low-dimensional lattices, leading to investigations of competing Kitaev and Heisenberg or Gamma interactions on quasi-one-dimensional chains or ladders [5] [26] [27] [28].

For instance, in 2018, C.E. Agrapidis et al. presented the phase diagram of the Kitaev-Heisenberg (KH) model on a one-dimensional chain. A comparison of the phase diagrams for the one-dimensional chain and the honeycomb-lattice KH model is shown on the left side of Figure 1.7. These phase diagrams reveal some deviations between the two lattice types. The visualization of the six ground states of the one-dimensional chain is displayed on the right side of Figure 1.7, with one phase (Tomonaga-Luttinger-liquid phase) exhibiting no long-range order but strong antiferromagnetic fluctuations [5]. The phase diagram shows that with pure Kitaev interactions, the one-dimensional chain should exhibit no long-range order. Additionally, when the Gamma interaction is included, the phase diagram of the Kitaev-Heisenberg-Gamma model on the one-dimensional chain shows a total of eleven different ground states [28].

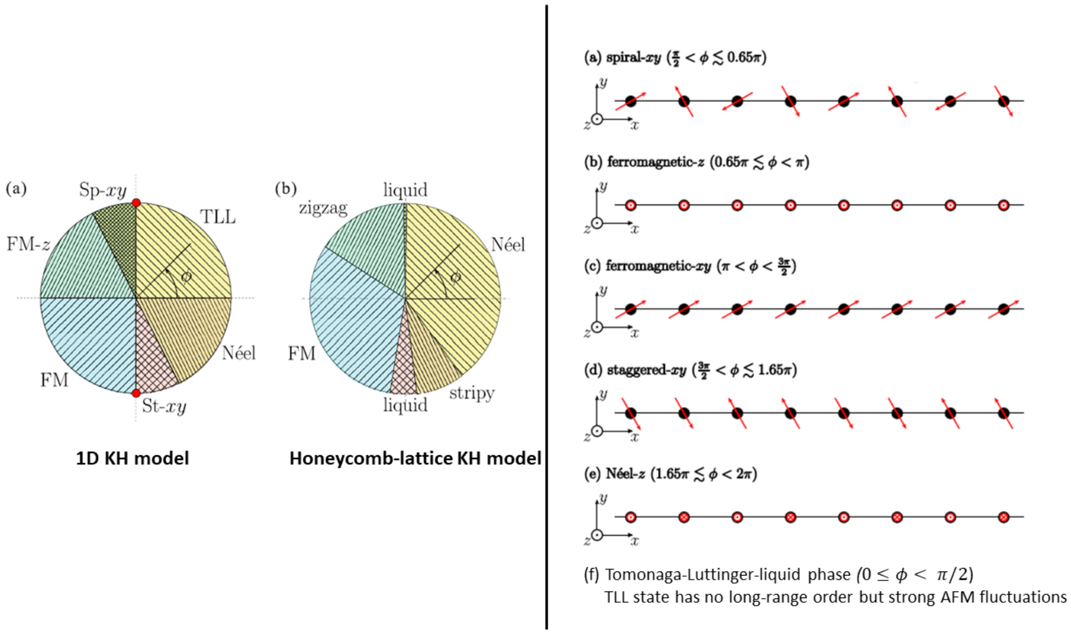

FIGURE 1.7: Left: A comparison of the ground-state phase diagrams between the one-dimensional chain and the honeycomb-lattice KH model. Right: Visualization of the six ground states realized in the 1D KH model with Kitaev and exchange couplings: $K = \sin\phi, J = \cos\phi$. Figure from [5]

However, experimental realizations of quasi-one-dimensional Kitaev chains remain limited. Only one potential candidate, $CoNb_2O_6$, featuring twisted one-dimensional chains, exhibits antiferromagnetic ordering of ferromagnetic chains under ambient conditions. Nonetheless, the long-range order can be suppressed with a transverse field, and the experimental data can be effectively described by a twisted Kitaev chain model [29]. It is evident that additional quasi-one-dimensional Kitaev systems are needed to test the theoretical predictions. This motivation drove our experimental interest in searching for alternative experimental realizations of other potential quasi-one-dimensional Kitaev chains.

Chapter 2

Experimental Techniques

2.1 Sample Synthesis

This project involves synthesizing high-quality samples of nominal Ca_2IrO_4, $Ca_5Ir_3O_{12}$, and yttrium-doped $Ca_5Ir_3O_{12}$ in both polycrystalline and single crystal forms using the following synthesis techniques.

Solid State Reaction

The polycrystalline samples were synthesized at the Brockhouse Institute for Materials Research's (BIMR) Centre for Crystal Growth at McMaster University. The solid-state reaction method was used, involving the synthesis of materials at temperatures below the melting points of reagents. High-quality reagents were accurately weighed to achieve the desired stoichiometry. The reagent mixture was manually ground in an agate mortar with acetone to enhance homogeneity. Once the acetone had fully evaporated, the resulting dry powder was pressed into 8mm pellets using a hydrostatic press at 20MPa pressure. These pellets were then placed in a 30ml ceramic crucible and heated in a box furnace or tube furnace, typically within the temperature range of 800 to 1300 °C. The synthesis process lasted from 1 to 7 days, with a heating and cooling rate of 60-100 °C/hour, and intermediate grinding and re-pelleting steps were applied.

Flux Growth Method

The single crystal samples were synthesized at the BIMR's Centre for Crystal Growth using the flux growth method. This technique involves mixing the reagents with an excess of low-melting-point flux. The mixture is then heated above the melting point of the flux and gradually cooled, allowing crystals to form. The desired amount of starting material was carefully weighed, and the flux was added in a 1:5 to 1:7 mass ratio of sample to flux. For synthesizing calcium iridates in this project, we typically used $CaCl_2$ as the flux. Both the starting material and flux were thoroughly mixed in an agate mortar before being placed and sealed in a 30ml platinum crucible. To ensure safety and prevent potential flux leakage, we wrapped the platinum crucible in alumina fiber and placed it inside a larger ceramic crucible. It was then heated in a box furnace, with the temperature gradually increasing at a rate of 60°C per hour. Once the target temperature was reached, the sample was slowly cooled to a temperature above the flux's melting point and then further cooled to room temperature at a rate of 60°C per hour. At room temperature, the flux was dissolved in ethanol, allowing single crystals to be separated and collected.

2.2 X-ray Diffraction

The structural information of the reacted samples is determined using two types of X-ray diffraction techniques.

Powder X-ray diffraction analysis was conducted at McMaster University. The reacted samples, were ground and then affixed to a silicon zero-background plate using a solution of petroleum jelly and Tollens solution. Powder X-ray diffraction was carried out using a PANalytical X'pert PRO diffractometer, covering an angle range from 20° to 80° in 2θ. Cu $K_{\alpha 1}$ radiation ($\lambda = 1.541$Å) was used as the X-ray source, and a germanium monochromator was used to eliminate the Cu $K_{\alpha 2}$ radiation. A point detector was used for data collection. The resulting XRD data were analyzed through Rietveld refinement in the Fullprof software to determine the phase purity and lattice parameters of the samples [30].

Single crystal X-ray diffraction was conducted at the McMaster Analytical X-ray Diffraction Facility (MAX) to obtain more detailed structural information on single crystal samples. A piece of single crystal sample, smaller than half a micron, was selected after crushing it, and this piece was attached to a glass fiber using GE varnish. The single crystal X-ray diffraction analysis was performed at room temperature using two diffractometers. The first one is the STOE IPDS II instrument with a molybdenum source ($\lambda = 0.709Å$), a graphite monochromator, and an image plate detector. The second one is the Bruker D8 Venture Duo equipped with a molybdenum source and a PHOTON III photon counting detector. The absorption correction and initial structure determination were carried out using the APEX4 Bruker Program [31]. Then, using Olex2 [32], the structure was solved with the SHELXT [33] structure solution program using intrinsic phasing and refined with the SHELXL [34] refinement package using least squares minimization.

2.3 Magnetization Characterization

Magnetic susceptibility measurements were conducted at McMaster University using a Quantum Design MPMS 5 RF SQUID magnetometer. This technique is used to investigate magnetic ordering. Both Zero Field Cooled (ZFC) and Field Cooled (FC) measurements were performed.

In the ZFC measurement, the sample was cooled without applying a magnetic field. Subsequently, a magnetic field (B) was applied, and the magnetization (M) was measured as the sample warmed to the target temperature, allowing the determination of the magnetic susceptibility ($\chi = \frac{M}{B}$). In contrast, in the FC measurement, the sample was cooled with a magnetic field applied, and the magnetization of the sample was then measured as the temperature increased. When cooling in the absence of a magnetic field (in ZFC), spins will align with no preferred orientation. On the other hand, when cooling with a magnetic field (FC), spins tend to align in the direction of the applied field, resulting in a difference between ZFC and FC susceptibility. The split in the ZFC and FC data can provide insights into the magnetic ground states of the sample, such as formation of magnetic domains, referring to regions within a material where the magnetic moments align, or spin glass, where the magnetic moments freeze randomly below the freezing temperature.

The quasi-one-dimensional calcium iridates exhibit anisotropic behavior, necessitating the study of magnetic properties in two primary directions: one with the magnetic field perpendicular to the c-axis and the other with it parallel to the c-axis. A few milligrams of phase-pure single crystals were selected. These crystals typically have a rod or needle-like shape, reflecting their crystallographic orientation. In this case, the c-axis aligns with the rod or needle. To ensure proper alignment, the crystals were visually oriented under a microscope. We secured the crystals in place using GE varnish and sandwiched them between two Kapton tapes. The crystal was then placed in a plastic straw, ensuring alignment along the desired direction of interest. Magnetization measurements were conducted using a SQUID magnetometer over a temperature range from 2K to 300K. Subsequently, we rotated the sample-Kapton assembly to measure the magnetic properties in another direction of interest. This approach ensures the use of the same crystals for each measurement and maintains the consistency of the diamagnetic background resulting from the GE varnish and sample holder. Furthermore, for the measurements presented in this paper, we used the Reciprocating Sample Option (RSO) mode, involving rapid oscillation of the sample at a known frequency while the SQUID detects the magnetic signals. This method allows for the differentiation of the sample signal from noise, making it highly sensitive to small magnetic moments.

If we assume the $J_{\text{eff}} = 1/2$ model in O_h symmetry, the high-temperature paramagnetic region of the susceptibility data can be fitted by the Curie–Weiss law with a temperature-independent term χ_0 to account for potential diamagnetic contributions and the nonmagnetic Ir^{5+} term.

$$\chi = \frac{C}{T - T_{CW}} + \chi_0 \tag{2.3.1}$$

The effective moment can be calculated using:

$$\mu_{\text{eff}} = g\sqrt{J(J+1)}\mu_B \tag{2.3.2}$$

where $g = \frac{3}{2} + \frac{S(S+1)-L(L+1)}{2J(J+1)}$, and in the $J_{\text{eff}} = 1/2$ model, Ir^{4+} has $\mu_{\text{eff}} = 1.73\mu_B$ and Ir^{5+} has $\mu_{\text{eff}} = 0$.

The Curie-Weiss temperature T_{CW}, which indicates the type and strength of the interaction, was estimated by fitting the experimental data to the inverse of susceptibility:

$$\chi^{-1} = \frac{T - T_{CW}}{C + \chi_0 \cdot (T - T_{CW})} \tag{2.3.3}$$

The magnetic moment μ_{eff} in units of Bohr magnetons was estimated using the Curie constant C:

$$\mu_{\text{eff}} = \sqrt{\frac{3k_B\chi}{N_A\mu_B^2 T}} = \sqrt{\frac{3k_B C}{N_A\mu_B^2}} \approx \sqrt{8C}\,\mu_B\,[\text{cgs}] \tag{2.3.4}$$

where k_B is the Boltzmann constant ($k = 1.3807 \times 10^{-16}$ erg/K), N_A is Avogadro's constant ($N_A = 6.0221 \times 10^{23}$ mol^{-1}), and μ_B is the Bohr Magneton ($\mu_B = 9.2741 \times 10^{-21}$ erg/G).

2.4 X-ray Absorption Spectroscopy

The electronic properties including Ir valence, crystal electric field effects, and the strength of spin-orbit coupling can be probed using X-ray absorption spectroscopy.

High energy resolution fluorescence detected X-ray absorption spectroscopy (HERFD-XAS) was carried out at the PIPOXS (ID2A) beamline at the Cornell High Energy Synchrotron Source, with measurements taken at both the Ir L_3 (11.21 keV) and L_2 (12.82 keV) edges. To select the energy of the incident X-ray beam, a silicon-(3,1,1) double crystal monochromator was used, with higher harmonic contributions suppressed by Rh-coated mirrors. Five spherical (1m radius) analyzers crystals were used, silicon-(8,0,0) for L_3 measurements (9.175 keV) and germanium-(8,8,0) for L_2 measurements (12.513 keV), and they were arranged in Rowland geometry. The data was collected using a Pilatus 100K detector while keeping the samples at 80K.

It is important to note that for studying 5d transition metals, which have broader spectra due to their shorter core-hole lifetimes, higher resolution is required. Unlike conventional XAS, which measures all emitted photons, HERFD-XAS utilizes analyzer crystals to select a particular final energy for emitted photons from a specific excited state. This improves HERFD-XAS resolution to around 3 eV, whereas conventional XAS at the Ir L3 edge has about 5 eV resolution.

The X-ray absorption spectroscopy data is typically divided into three regions. First, the pre-edge region, characterized by a featureless spectrum due to insufficient energy to excite core electrons to higher bands. This region primarily serves for normalization purposes. The second region is the X-Ray Absorption Near Edge Structure (XANES) region. It exhibits two key features: the "white-line" feature, a sharp energy peak corresponding to core electron excitation to the conduction band, and the edge step region, where energy is sufficient to excite core electrons to the continuum. The third region is the Extended X-ray Absorption Fine Structure (EXAFS) region. It captures oscillations caused by ionized electrons scattering with their electron cloud environment, providing information about the neighboring atomic environment of the absorbing atom. In this paper, we focus only on the XANES region. The analysis of EXAFS is beyond the scope of this paper, and it is primarily used for normalization alongside the pre-edge region.

XAS serves as a tool to estimate the oxidation state of a material. Both edge and "white-line" feature energies tend to rise with an increasing oxidation state, as core electrons move closer to the positively charged nucleus, requiring more energy for ionization. The splitting of the L_3 "white-line" feature provides information about the 10Dq t_{2g} to e_g splitting, while the intensity of the "white-line" feature can offer insights into spin-orbit interactions.

In the fluorescence mode used, the linear X-ray attenuation coefficient ($\mu(E)$) is proportional to the ratio of fluorescence intensity (I_f) to the incident intensity (I_o) of the X-ray beam passing through the sample. Raw data undergoes normalization in the ATHENA program. This involves fitting a linear line to the pre-edge and a quadratic polynomial to the post-edge EXAFS region to normalize both L_2 and L_3 data from 0 (pre-edge) to 1 (post-edge). Then, the absorption edge is fitted with both step and arctangent functions. Gaussian functions are also employed to fit the XANES region to extract peak positions and integrated intensities. Importantly, as depicted in Figure 2.1, the arctangent function offers a better fit. While the quantitative outcomes from the two fits may differ, the qualitative trends with respect to doping levels remain consistent.

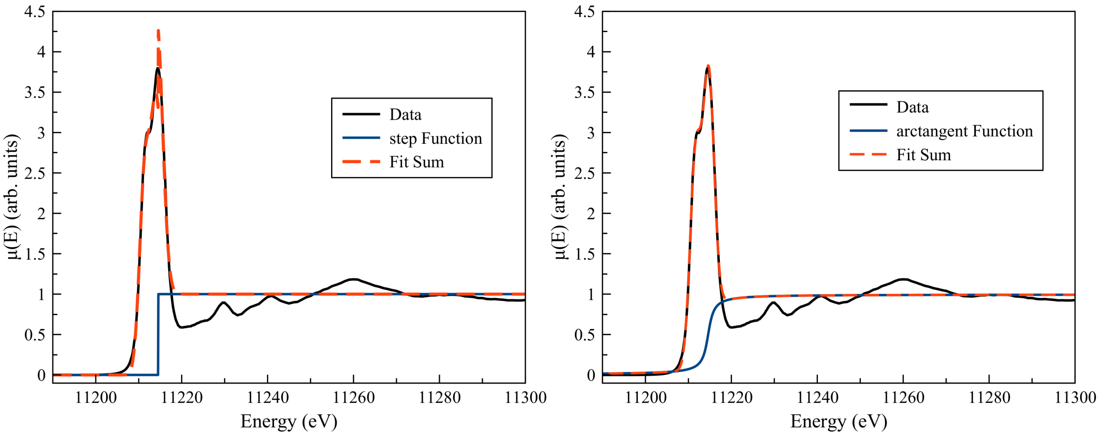

FIGURE 2.1: X-ray attenuation coefficient ($\mu(E)$) vs. energy for two different fits. The black line represents the normalized $\mu(E)$, the blue line represents the step or arctan function used for fitting the absorption edge, and the red dashed line shows the fitted sum.

Then, the branching ratio (BR), under the assumption of negligible spin-orbit coupling [35], can be calculated as follows:

$$\begin{aligned}\frac{I_{L3}}{I_{L_3}+I_{L_2}} &= \frac{2}{3}+\frac{\langle L\cdot S\rangle}{3\langle n_h\rangle}\\ \frac{I_{L3}}{I_{L_3}+I_{L_2}} &= \frac{2}{3}\\ BR = \frac{I_{L3}}{I_{L_2}} &= 2\end{aligned} \tag{2.4.1}$$

The spin-orbit expectation value ($\langle L\cdot S\rangle$) can be estimated from experimental data:

$$\begin{aligned}\frac{I_{L3}}{I_{L_3}+I_{L_2}} &= \frac{2}{3}+\frac{\langle L\cdot S\rangle}{3\langle n_h\rangle}\\ \langle L\cdot S\rangle &= 3\langle n_h\rangle(\frac{I_{L3}}{I_{L_3}+I_{L_2}}-\frac{2}{3})\end{aligned} \tag{2.4.2}$$

Chapter 3

Attempted Material Synthesis and Characterization of Ca_2IrO_4

This chapter presents the attempted synthesis of Ca_2IrO_4 in both polycrystalline and single crystal forms. In spite of significant effort, the results obtained from the structural and magnetic characterization closely align with the Ca-deficient $Ca_5Ir_3O_{12}$ compound rather than the intended Ca_2IrO_4 composition for all samples.

3.1 Introduction

In the search for experimental realizations of the low-dimensional Kitaev chain, which satisfies the two criteria proposed by G. Jackeli and G. Khaliullin, described in Chapter 1, Ca_2IrO_4 has emerged as a promising candidate. The Ca_2IrO_4 compound contains pure Ir^{4+} ions centered in oxygen octahedra, that potentially exhibit a $J_{\mathrm{eff}} = 1/2$ ground state. This aligns with the first criterion for realizing Kitaev interactions. In Ca_2IrO_4, IrO_6 octahedral cages form edge-sharing chains, and the metal-oxygen-metal (TM-O-TM) bond angles are around 103^o-105^o [36], which is close to the proposed 90^o bond geometry in the second criterion for minimizing the Heisenberg interaction.

The compound Ca_2IrO_4 was first reported by D. Babel et al. in 1966, with the space group $P\bar{6}2m$ and lattice parameters of $a = b = 9.42$Å and $c = 3.19$Å [36]. Later, a study by R.F. Sarkozy et al. in 1974 characterized Ca_2IrO_4 as a semiconductor and reported a discontinuity in the inverse magnetic susceptibility at 90K, interpreted as the development of antiferromagnetic order [37]. It is important to note that this result deviates from the spin-orbital Mott insulator behavior expected for Ir^{4+} in the modern $J_{\text{eff}} = 1/2$ picture.

Nevertheless, more recent research by F.J.J. Dijksma et al. in 1993 challenged the earlier structural identifications, proposing that the correct structure is $Ca_5Ir_3O_{12}$, a Ca-deficient version of Ca_2IrO_4. Both compounds share the same space group and comparable lattice parameters [38]. Notably, while Ca_2IrO_4 consists of pure Ir^{4+} valence, $Ca_5Ir_3O_{12}$ has a mixed valence of $Ir^{4.67+}$ with an Ir^{4+}:Ir^{5+} ratio of 1:2. The $Ca_5Ir_3O_{12}$ compound demonstrates a metal-insulator transition around room temperature, an antiferromagnetic transition at 7.8K in magnetic susceptibility measurements, and a distinct anomaly around 105K in specific heat measurements [39][40]. The origin of this high-temperature nonmagnetic anomaly remains unknown, but subsequent studies have suggested its potential connection to electric toroidal ordering [41] [42].

Despite the structural discrepancy between Ca_2IrO_4 and $Ca_5Ir_3O_{12}$, recent studies continue to report the Ca_2IrO_4 structure. For example, Hk Muller-Buschbaum in 2003 reviewed the crystal chemistry of Ca_2IrO_4 structure [43], N. Keawprak et al. in 2009 reported the synthesis and experimental thermoelectric properties of Ca_2IrO_4 [44], and V. Singh and J.J. Pulikkotil in 2018 conducted a computational study of the electronic structure and magnetic properties of Ca_2IrO_4 [45].

Given the structural similarities between Ca_2IrO_4 and $Ca_5Ir_3O_{12}$, and some of the discrepancies between previous characterization measurements, it is important to determine whether the synthesis of Ca_2IrO_4 is feasible or if $Ca_5Ir_3O_{12}$ is the only stable phase. This can be achieved through structural and magnetic characterization of the synthesized material, and ensuring that the material synthesized contains only Ir^{4+} ions forming edge-sharing octahedral chains, thereby ensuring the suitability of the material for a quasi-one-dimensional Kitaev chain model.

3.2 Synthesis and Characterization of Powder Samples

3.2.1 Phase Identification and Crystal Structure

The initial step in phase identification involves distinguishing between Ca_2IrO_4 and $Ca_5Ir_3O_{12}$. Figure 3.1 (a) presents the (001) projection of both the Ca_2IrO_4 and $Ca_5Ir_3O_{12}$ structures, generated using PowderCell. Notably, these structures share significant similarities; however, $Ca_5Ir_3O_{12}$ differs by containing a calcium vacancy at the (0,0,0) position. Additionally, Figure 3.1 (b) displays the theoretically calculated X-ray diffraction (XRD) patterns of Ca_2IrO_4 and $Ca_5Ir_3O_{12}$ using PowderCell [46]. These patterns show minimal differences, primarily seen in two weak peaks. $Ca_5Ir_3O_{12}$ shows a stronger (2,1,0) peak, while Ca_2IrO_4 shows a more pronounced (1,0,1) peak. Therefore, distinguishing between the two phases through powder XRD patterns is challenging. Identifying phase pure Ca_2IrO_4 with this technique primarily relies on the absence of residual starting materials or other impurities in the synthesized samples.

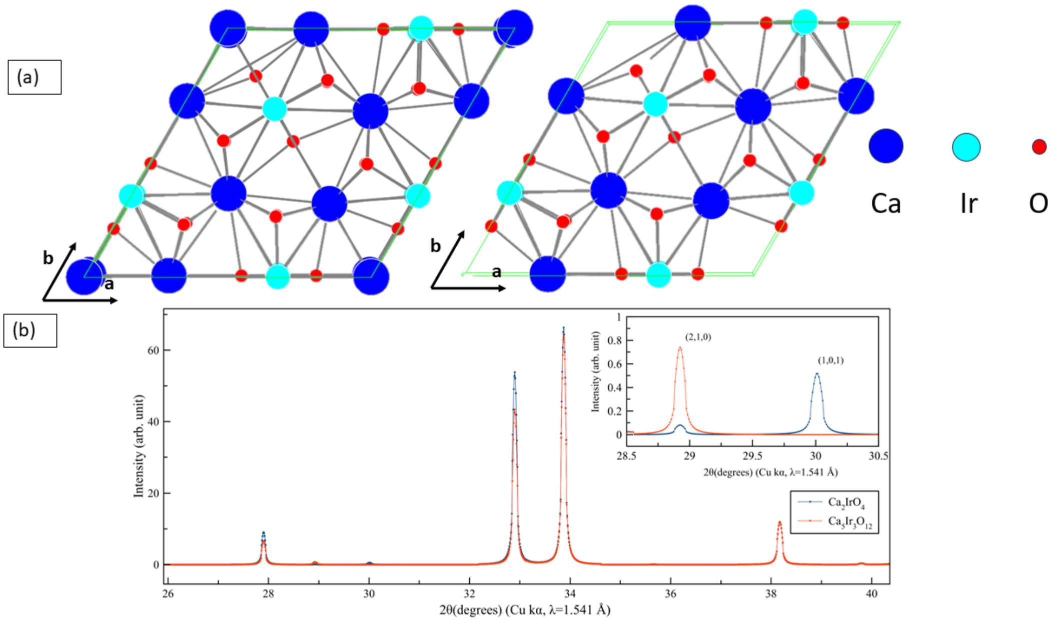

FIGURE 3.1: (a) (001) projection of Ca_2IrO_4 (left) and $Ca_5Ir_3O_{12}$ (right). (b) Calculated Ca_2IrO_4 and $Ca_5Ir_3O_{12}$ powder XRD pattern using $\lambda = 1.541$Å.

3.2.2 Synthesis and Structural Characterization of Powder Samples

Attempts were made to synthesize a polycrystalline sample of nominal Ca_2IrO_4 using solid-state reaction in two environments, O_2 and Ar. Notably, different impurity phases were observed under these distinct environments, although no significant variation was observed for different temperature profiles within the same environment.

Solid state synthesis and structural characterization of nominal Ca_2IrO_4 in O_2 environment

The nominal Ca_2IrO_4 polycrystalline sample was first synthesized in an O_2 environment using the solid-state reaction method, following the temperature profile described by D. Babel et al. [36] and C.L. McDaniel et al. [47].

The starting materials, $CaCO_3$ and IrO_2, were mixed in a 2:1 molar ratio, and the resulting mixture was ground and pressed into a pellet using the method described in Chapter 2. Then, the pellet was fired in an O_2 environment at temperatures ranging from 800°C to 1100°C, over 1 to 3 days, with intermediate grinding and pelleting.

Various temperature profiles were used for synthesizing polycrystalline samples of nominal Ca_2IrO_4. Among these attempts, two specific profiles are presented in Figure 3.2, showing the typical outcomes of these growths under the O_2 environment. These growths consistently exhibited a 4-7% CaO impurity, as shown in Figures 3.2 (a) and (c).

The presence of the CaO impurity raised concerns that not all calcium atoms were fully incorporated into the final product, possibly leading to a calcium-deficient phase, most likely $Ca_5Ir_3O_{12}$. Considering the possibility that the formation of the CaO impurity might be more energetically favorable in an O_2-rich environment, the synthesis of nominal Ca_2IrO_4 was replicated in an Ar environment with the same temperature profile.

Solid state synthesis and structural characterization of nominal Ca_2IrO_4 in Ar environment

The synthesis of the nominal Ca_2IrO_4 polycrystalline sample was replicated in an Ar environment, following the identical temperature profile used in the O_2 environment for direct comparison. Stoichiometric amounts of $CaCO_3$ and IrO_2 were mixed, pressed into a pellet, and fired in a tube furnace. Initially, O_2 was removed at 60°C for 2 hours, after which the pellet was fired using the O_2 environment temperature profile.

Figures 3.2 (b) and (d) show the XRD patterns obtained when using the Ar environment with the same temperature profiles. These figures show the presence of a 30-60% Ca_4IrO_6 impurity. This suggests that Ca_4IrO_6 is more likely to form in an oxygen-deficient environment, indicating the unsuitability of the Ar environment for synthesizing nominal Ca_2IrO_4. Furthermore, none of the XRD patterns in Figure 3.2 show a (1,0,1) peak, further indicating the absence of the desired Ca_2IrO_4 phase.

Hence, it is evident that different temperature profiles under the same environment yield the same impurity phase, while different environments, O_2 and Ar, result in different impurity phases, CaO and Ca_4IrO_6, respectively. The polycrystalline samples synthesized under the Ar environment are clearly non-single phase due to the presence of the Ca_4IrO_6 impurity. While the samples synthesized under the O_2 environment are closer to single phase, it is still difficult to determine the structure of the synthesized sample with powder XRD characterization alone, further characterization using other techniques is required.

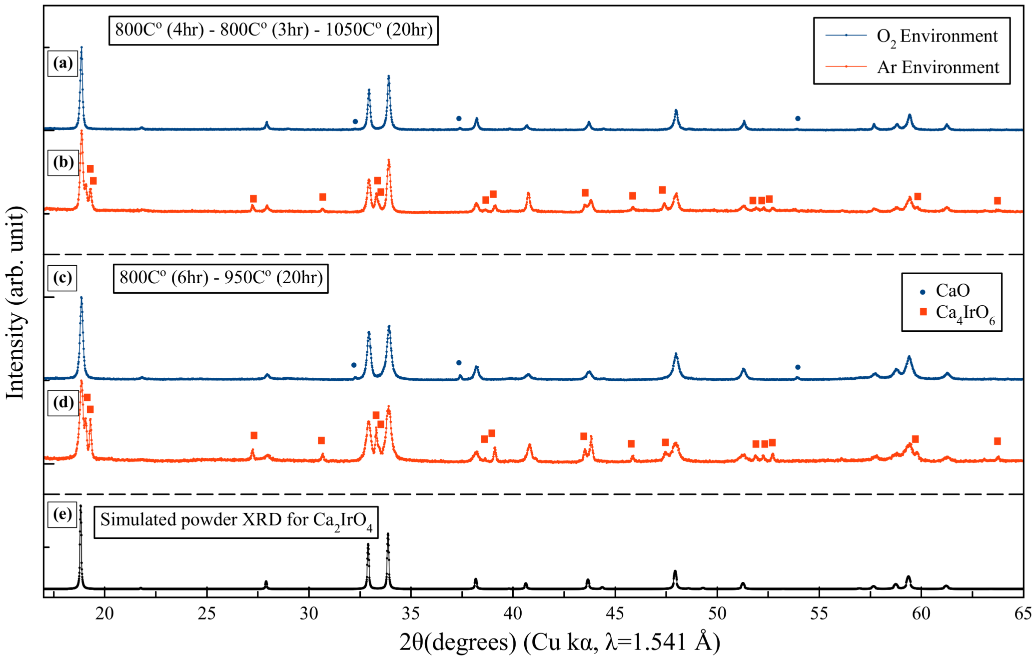

FIGURE 3.2: Powder XRD data of Ca_2IrO_4 materials synthesized using two distinct temperature profiles under O_2 and Ar environments. (a) and (b) present results under one temperature profile (annealing temperature (duration)), while (c) and (d) correspond to another. In panels (a) and (c), samples were synthesized under an O_2 environment showing the CaO impurity. In panels (b) and (d), samples were synthesized under an Ar environment showing the Ca_4IrO_6 impurity. (e) shows the simulated powder XRD pattern of pure Ca_2IrO_4 for comparison.

3.2.3 Magnetic Characterization of nominal Ca_2IrO_4 in O_2 Environment

For further characterization of the synthesized material in the O_2 environment mentioned above, magnetic susceptibility measurements were conducted using a SQUID magnetometer as described in Chapter 2. Figure 3.3 presents the zero field cooled (ZFC) and field cooled (FC) susceptibility data with 100Oe applied field, depicting a clear transition around 7.5(5)K, consistent with the reported 7.8K transition temperature for $Ca_5Ir_3O_{12}$ [39][40]. Notably, no discontinuity was observed in the inverse of susceptibility around 90K as reported by R.F. Sarkozy et al. for Ca_2IrO_4 [37]. This combination of structural and magnetic characterizations conclusively confirms that the material obtained through solid-state reaction under the O_2 environment is not Ca_2IrO_4.

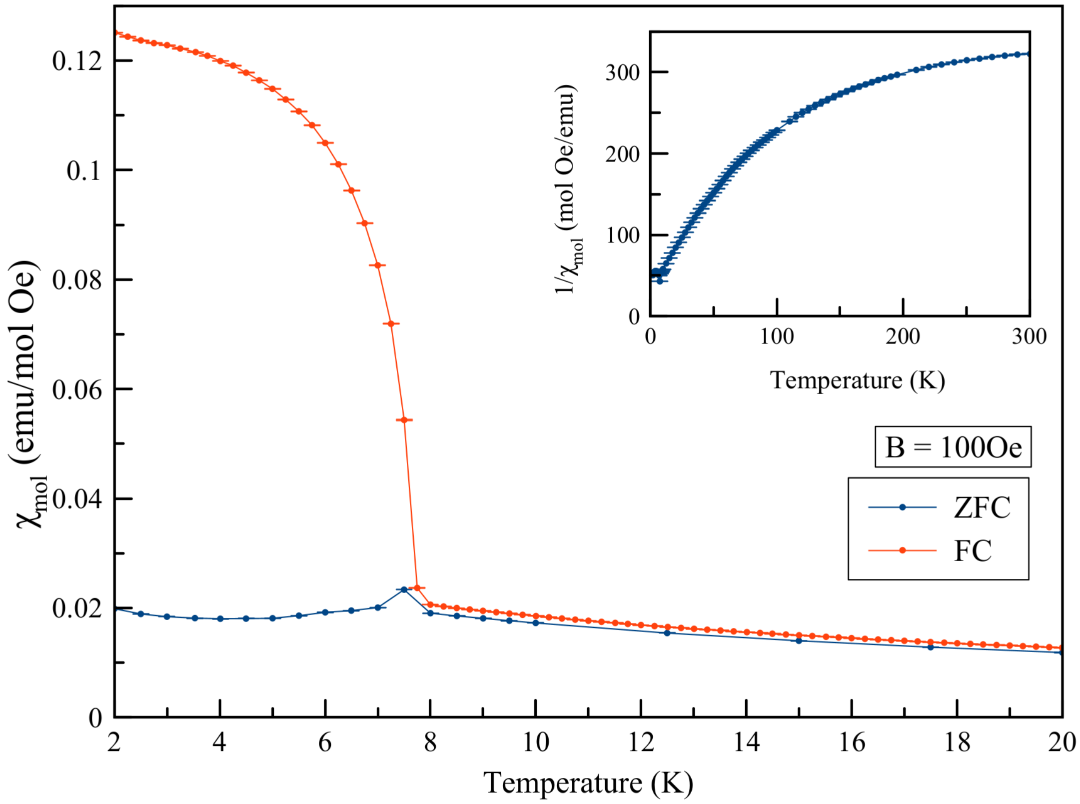

FIGURE 3.3: Zero field cooled (ZFC) and field cooled (FC) susceptibility with an applied field of B=100Oe for Ca_2IrO_4 synthesized under O_2 environment, showing a transition around 7.5(5)K. The inverse susceptibility plot displays no discontinuity around 90K.

3.3 Synthesis and Characterization of Single Crystal Samples

Since achieving phase-pure powder samples was unsuccessful, the focus shifted to synthesizing single crystal samples. The single crystal samples of nominal Ca_2IrO_4 were synthesized using the flux growth method, using two different fluxes from previous literature: Na_2CO_3 [36] and $CaCl_2$ [40].

3.3.1 Synthesis of Single Crystal Samples

Single crystal synthesis of nominal Ca_2IrO_4 with Na_2CO_3 as flux

Initially, an attempt was made to synthesize single crystals of Ca_2IrO_4 using the flux growth method, following the procedure described by D. Babel et al. [36]. The starting material consisted of stoichiometric amounts of $CaCO_3$ and IrO_2, with Na_2CO_3 added as a flux in a 1:7 sample-to-flux molar ratio. The mixture was fired in a box furnace, with the temperature raised to 950°C for 1 hour, and cooled down to 650°C at a rate of 6°C/h, followed by a final cooling to room temperature at a rate of 60°C/h.

The obtained material exhibited characteristics resembling a ‘melt cake’ as described in the paper by D. Babel et al. However, after dissolving the ‘melt cake’ in HCl as described in their paper, no single crystals were observed.

Single crystal synthesis of nominal Ca_2IrO_4 with $CaCl_2$ as flux

Subsequently, another attempt was made to synthesize single crystals of nominal Ca_2IrO_4 using the flux growth method described by G. Cao et al. for synthesizing other calcium iridates phases like $Ca_5Ir_3O_{12}$ and Ca_4IrO_6 [40]. Stoichiometric amounts of $CaCO_3$ and IrO_2 were mixed, and $CaCl_2$ was added as the flux in a 1:7 sample-to-flux molar ratio. The mixture was sealed in a platinum crucible and fired in a box furnace at 1330°C for a duration of 4 hours. Then, it was cooled down to 1200°C at a rate of 2°C/h, followed by a final cooling to room temperature at a rate of 100°C/h. After dissolving the flux in ethanol, single crystals were successfully obtained.

The single crystals of nominal Ca_2IrO_4 generally had a rod-like shape, which is indicative of quasi-one-dimensional characteristics, and a hexagonal cross-section reflecting 6-fold crystal symmetry as shown in Figure 3.4. To further analyze the crystal structure and chemical composition, one of the crystals was selected for single crystal X-ray diffraction measurements.

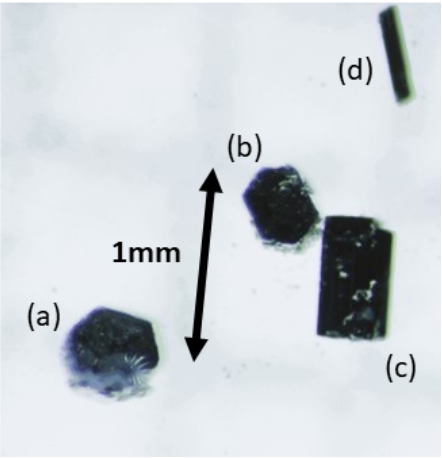

FIGURE 3.4: Single crystals of nominal Ca_2IrO_4 obtained from the $CaCl_2$ flux growth method. The crystals typically exhibit a rod-like or needle-like shape with less than 1mm in length, as shown in (c) and (d), and a hexagonal cross-section, as shown in (a) and (b).

3.3.2 Structural Characterization of Single Crystal Samples

Single crystal X-ray diffraction data was collected on a selected crystal using the STOE IPDS II X-ray diffractometer with molybdenum source (λ = 0.709Å). The refined crystallographic data are summarized in Table 3.1. During refinement, very small amounts of electron density were observed at the (0,0,0) position in the experimental data, as shown in Figure 3.5 by Q, the electron density difference between experimental data and the fitted model ($\rho_{exp} - \rho_{model}$). However, by including a calcium atom with refinable chemical occupancy at this site, the refinement yielded a chemical occupancy of 0.025 for calcium, indicating the experimental data only shows 2.5% of calcium electron density for a fully occupied site. Additionally, the magnitude of the electron density difference Q for the (0,0,0) site is approximately at the background noise level. Hence, we conclude that the refinable electron density at this site is negligible, and the final refined crystal structure obtained from the experiment is consistent with the chemical composition of $Ca_5Ir_3O_{12}$.

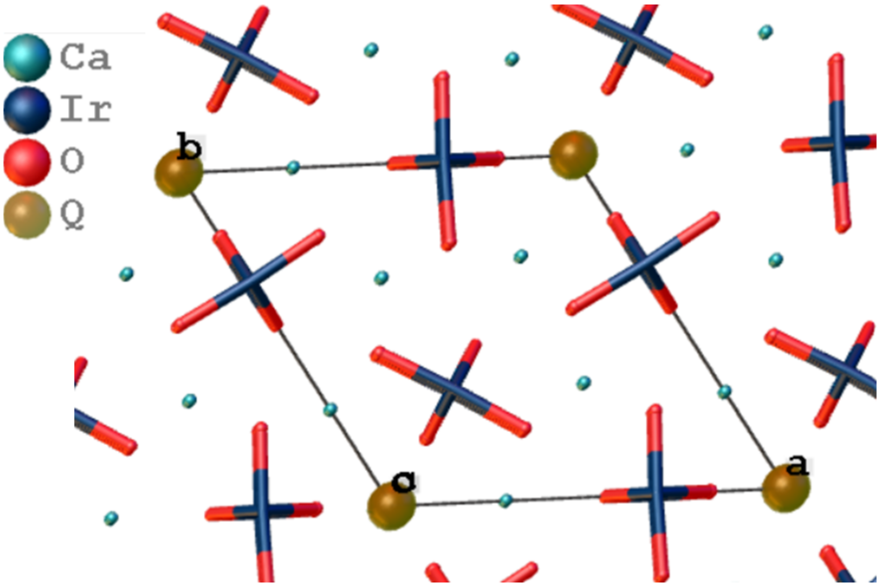

FIGURE 3.5: Ball-and-stick style representation of the (001) projection created using the single crystal refinement interface Olex2. In the figure, Q represents the electron density difference between experimental data and the fitted model ($\rho_{exp} - \rho_{model}$). The final refinement indicates negligible electron density at the (0,0,0) site, consistent with the crystal composition of $Ca_5Ir_3O_{12}$.

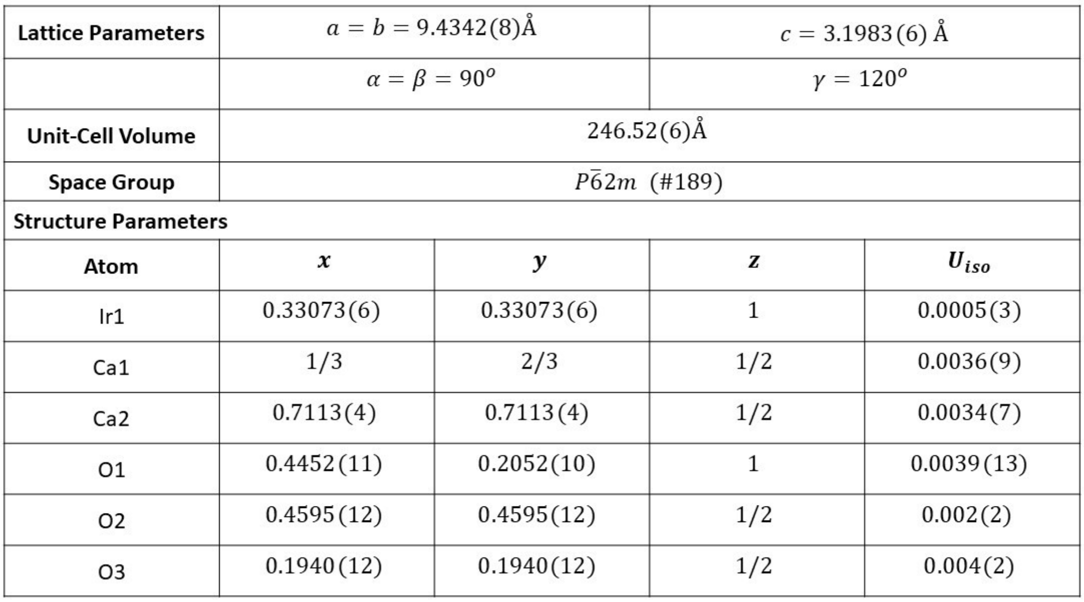

Lattice Parameters	$a = b = 9.4342(8)$Å		$c = 3.1983(6)$ Å	
	$\alpha = \beta = 90^o$		$\gamma = 120^o$	
Unit-Cell Volume	246.52(6)Å			
Space Group	$P\bar{6}2m$ (#189)			
Structure Parameters				
Atom	$\boldsymbol{x}$	$\boldsymbol{y}$	$\boldsymbol{z}$	$\boldsymbol{U_{iso}}$
Ir1	0.33073(6)	0.33073(6)	1	0.0005(3)
Ca1	1/3	2/3	1/2	0.0036(9)
Ca2	0.7113(4)	0.7113(4)	1/2	0.0034(7)
O1	0.4452(11)	0.2052(10)	1	0.0039(13)
O2	0.4595(12)	0.4595(12)	1/2	0.002(2)
O3	0.1940(12)	0.1940(12)	1/2	0.004(2)

Table 3.1: Selected crystallographic data from the refinement of single crystal X-ray diffraction.

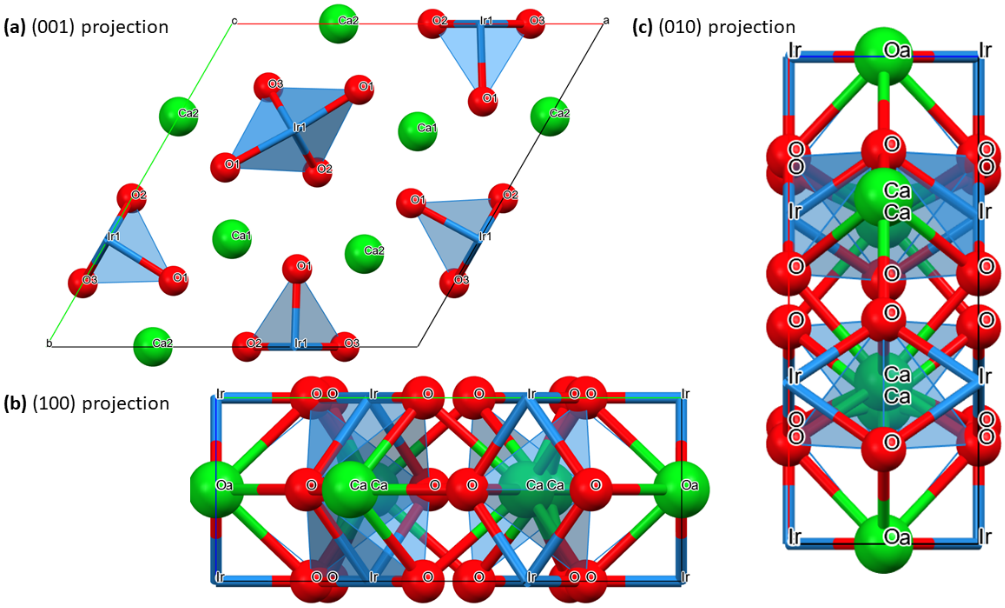

FIGURE 3.6: Ball and stick style representations of the refined crystal structure obtained from single crystal X-ray diffraction, displaying three projections. (a) shows the (001) projection with atom label consistent with Table 3.1, the absence of significant electron density at the (0,0,0) position is consistent with the composition of $Ca_5Ir_3O_{12}$. (b) and (c) show (100) and (010) projection respectively.

3.3.3 Magnetic Characterization of Single Crystal Samples

Another approach to verifying the composition of the sample involves characterizing its magnetic properties. Figure 3.7 presents magnetic susceptibility measurements with applied field along the c-axis of the crystals. The data show an anomaly at 7.4(5)K, and the Curie-Weiss temperature of $T_{CW} = -312(25)$K indicates a net antiferromagnetic interaction along the chain direction. This aligns closely with the reported antiferromagnetic transition temperature of 7.8K for $Ca_5Ir_3O_{12}$ [39][40]. The magnetic transition at this temperature implies that the material exhibits magnetic behavior consistent with $Ca_5Ir_3O_{12}$. Furthermore, the absence of the 90K anomaly described by R.F. Sarkozy et al. [37] provides additional evidence that the synthesis process resulted $Ca_5Ir_3O_{12}$

instead of the desired Ca_2IrO_4 phase.

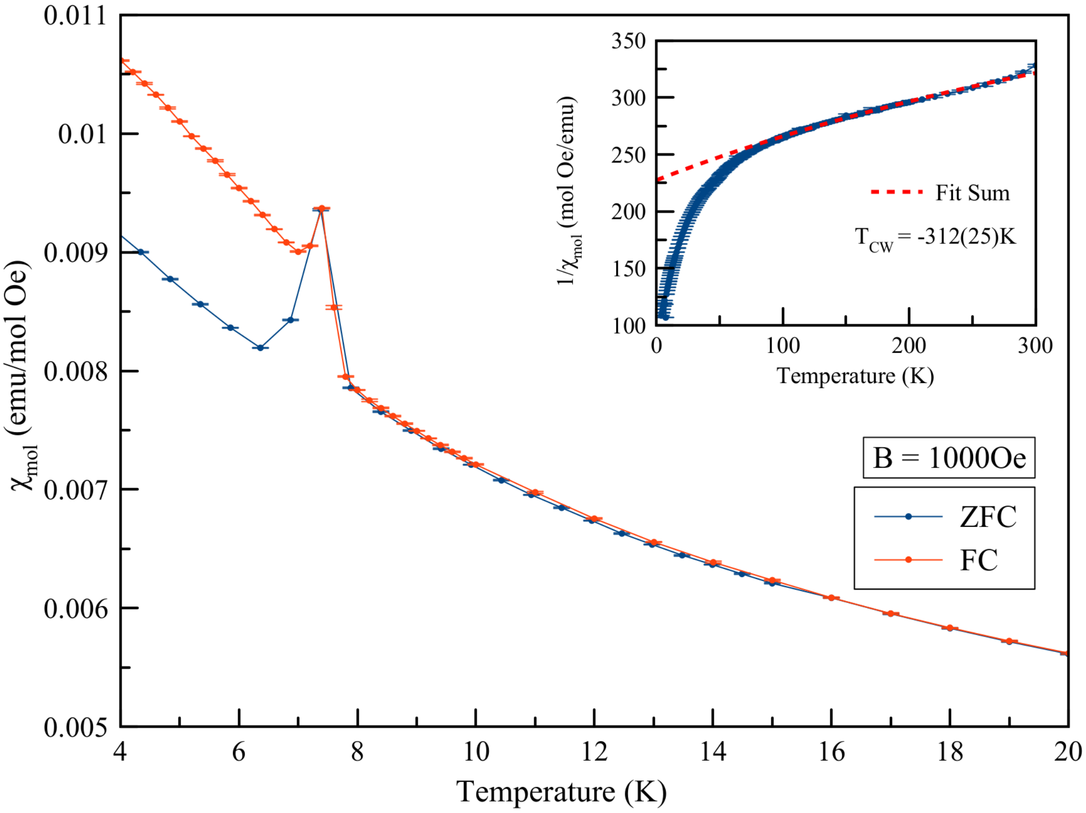

FIGURE 3.7: Zero field cooled (ZFC) and field cooled (FC) susceptibilities of nominal Ca_2IrO_4 single crystals with an applied field of $B = 1000$Oe along the c-axis of the crystal. The susceptibility plot shows an anomaly around 7.4(5) K. The inverse susceptibility plot includes a Curie-Weiss fit with a temperature-independent term in red. The Curie-Weiss temperature is determined by fitting the paramagnetic region above 150 K. Notably, the plot shows no discontinuity around 90K.

3.4 Conclusion

In conclusion, despite extensive efforts to synthesize Ca_2IrO_4 in both polycrystalline and single crystal forms, the material obtained was identified as $Ca_5Ir_3O_{12}$, a calcium-deficient phase of Ca_2IrO_4. Structural and magnetic characterization measurements revealed a lack of calcium at the (0,0,0) position and an antiferromagnetic transition around 7.4(5)K, consistent with $Ca_5Ir_3O_{12}$. While recent literature still refers to Ca_2IrO_4 [43][44][45], the results presented in this chapter confidently confirm that Ca_2IrO_4 cannot be synthesized under the reported conditions and methods, thus aligning with Dijksma's argument [38]. Consequently, we need to explore alternative materials for realizing the quasi-one-dimensional Kitaev chain.

Chapter 4

Material Synthesis and Characterization of Yttrium-doped $Ca_5Ir_3O_{12}$: $Ca_{5-x}Y_xIr_3O_{12}$

The previous chapter showed the synthesis of a stoichiometric Ca_2IrO_4 was unsuccessful, therefore failing to obtain pure Ir^{4+} chains necessary for realizing the quasi-one-dimensional Kitaev model. Instead, the existing structure of $Ca_5Ir_3O_{12}$ contains a mixed valence of Ir^{4+} and Ir^{5+} in a 1:2 ratio, resulting in an average Ir oxidation state of +4.67. To explore an alternative candidate for the low-dimensional Kitaev chain, we decided to tune the Ir oxidation state from $Ir^{4.67+}$ to Ir^{4+} through chemical doping.

This chapter discusses the synthesis of a series of yttrium-doped $Ca_5Ir_3O_{12}$ materials in both polycrystalline and single-crystal forms. The structural, magnetic, and electronic characterizations of these materials provide compelling evidence that the synthesis of the doped samples was successful. The highest doping level achieved ($x = 1.52$ or approximately 30% doping) is considerably higher than any previously studied doped $Ca_5Ir_3O_{12}$ systems.

4.1 Introduction

Previous studies have successfully demonstrated low-level chemical doping in $Ca_5Ir_3O_{12}$. For instance, in 2016 X. Chen et al. reported the isoelectronic doping of 11% Sr^{2+} in a single crystal, which exhibited a slightly elevated antiferromagnetic transition at 9K [48]. Furthermore, in 2019 S. Haneta et al. reported the hole-doping of 10% Na^{+}, as well as the electron-doping of 10% La^{3+} and Bi^{3+} in polycrystalline samples. The La^{3+} doped sample showed no change in the transition temperature, while the Bi^{3+} and Na^{+} doped samples exhibited a suppression of the 7.8K antiferromagnetic transition to 5K and 4K, respectively. However, X-ray diffraction data indicated the presence of IrO_2 and unidentified impurities in the latter two doped samples [49].

In our search for an appropriate carrier doping candidate to achieve a pure Ir^{4+} $J_{\text{eff}} = 1/2$ chain, we established three specific criteria. First, the dopant should add electrons to lower the oxidation state of Ir. Second, it should possess a similar ionic radius to that of Ca^{2+}, ensuring that the dopant does not exert excessive chemical pressure on the system, thereby enhancing the possibility of successful doping. Third, it should be nonmagnetic to avoid complicating the magnetic structure. We propose Y^{3+} as a promising candidate that meets these criteria, as it has an oxidation state higher than Ca^{2+}, and it has ionic radii similar to that of Ca^{2+}. For coordination numbers VII and IX, which correspond to $(x, x, 1/2)$ and $(1/3, 2/3, 1/2)$ positions in the context of $Ca_5Ir_3O_{12}$ (see Table 4.3), Ca^{2+} has ionic radii of 1.06Å and 1.18Å, respectively, while Y^{3+} has ionic radii of 0.96Å and 1.08Å, respectively[50]. Moreover, it is nonmagnetic. Thus, by introducing 40% Y^{3+} doping, i.e., $Ca_3Y_2Ir_3O_{12}$, the desired Ir^{4+} oxidation state can be achieved.

4.2 Material Synthesis and Structural Characterization

To the best of our knowledge, there is no previous literature on the synthesis of Y-doped $Ca_5Ir_3O_{12}$. The main challenge during the growth process was the elimination of the more favorable yttrium pyrochlore $Y_2Ir_2O_7$ impurity phase. Therefore, synthesizing phase-pure powder samples and single crystals required extensive trial and error before discovering the optimal methods.

4.2.1 Synthesis and Phase Identification of Polycrystalline Samples

The polycrystalline sample of Y-doped $Ca_5Ir_3O_{12}$ was prepared in an O_2 environment using the solid-state reaction method described in Chapter 2.

Stoichiometric amounts of $CaCO_3$, Ir metal, and Y_2O_3 were used as starting materials. Yttrium oxide was annealed at 1000°C overnight before weighing since yttrium oxide reacts with water from the environment to form yttrium (III) hydroxide. The reagent mixture was then weighed precisely to maintain the stoichiometric ratio and extensively ground to reduce the particle size of the starting materials. Subsequently, the mixed powder was pressed into a pellet and fired in a box furnace at 800°C over a duration of 2-3 days. Following this, the pellet was once again ground extensively and refired in the box furnace at temperatures ranging from 900°C to 1200°C over a period of 8-15 days, with intermediate grinding.

Figure 4.2 presents the temperature profile of a successful growth with a nominal doping level of $x = 0.5$. Notably, through multiple grinding and refiring steps at higher temperatures, both the starting materials IrO_2 and Y_2O_3, as well as the impurity phase $Y_2Ir_2O_7$, were effectively eliminated, resulting in a phase-pure sample.

Figure 4.1 displays the three most intense peaks from Figure 4.2. It is apparent that the (1,1,1) peak remains largely unchanged, while the (1,1,0) and (3,0,0) peaks have shifted by approximately 0.1° in 2θ. This shift corresponds to a change in lattice constants from the initial firing values of $a = b = 9.4017(3)$Å and $c = 3.1881(1)$Å to the final lattice constants of $a = b = 9.3780(4)$Å and $c = 3.1890(1)$Å. Consequently, there is a reduction in cell volume from $V = 281.8024(1)\text{Å}^3$ to $V = 280.4626(2)\text{Å}^3$. As stated in the introduction of this chapter, Y^{3+} ions have smaller radii compared to Ca^{2+} ions. Thus, a decrease in cell volume is expected with this doping. The observed reduction in lattice parameters, along with the absence of impurity phases, provides evidence of the successful incorporation of Y^{3+} dopant into the parent compound.

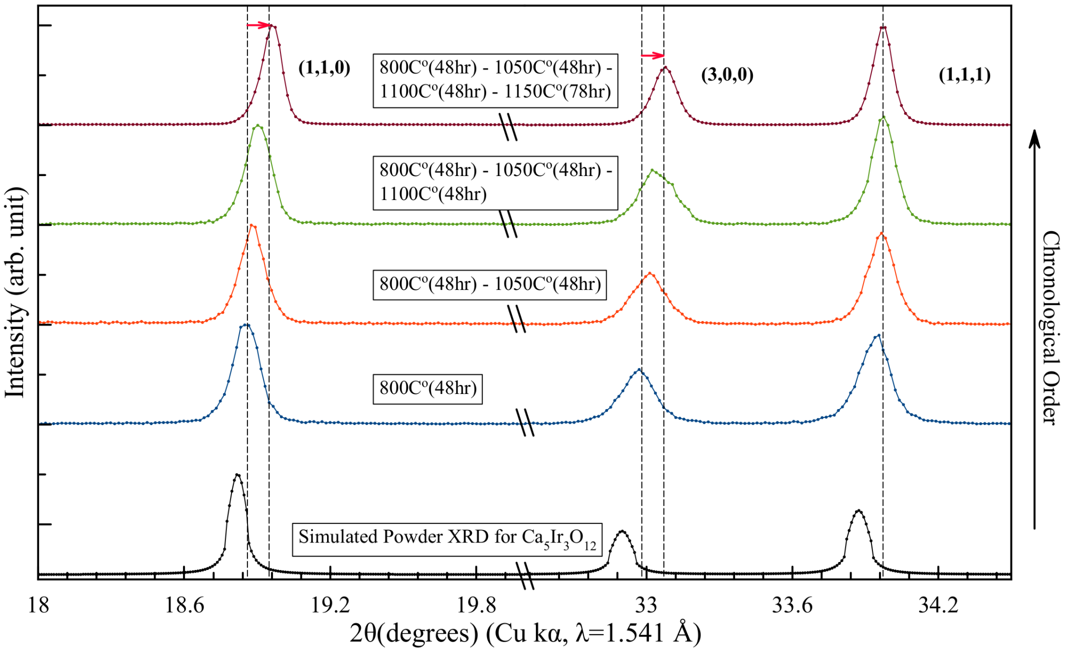

FIGURE 4.1: Zoomed-in view of Figure 4.2 that shows the shifts in (1,1,0) and (3,0,0) diffraction peaks, while the (1,1,1) diffraction peaks remaining unchanged. Dashed lines serve as a visual guide to indicate the peak shifts in each firing. The bottom panel displays a simulated powder XRD pattern for $Ca_5Ir_3O_{12}$ using $a = b = 9.42$Å, and $c = 3.19$Å as a comparison.

Similar results were observed for nominal doping levels of $x = 0.25, 0.5, 1, 2$. The

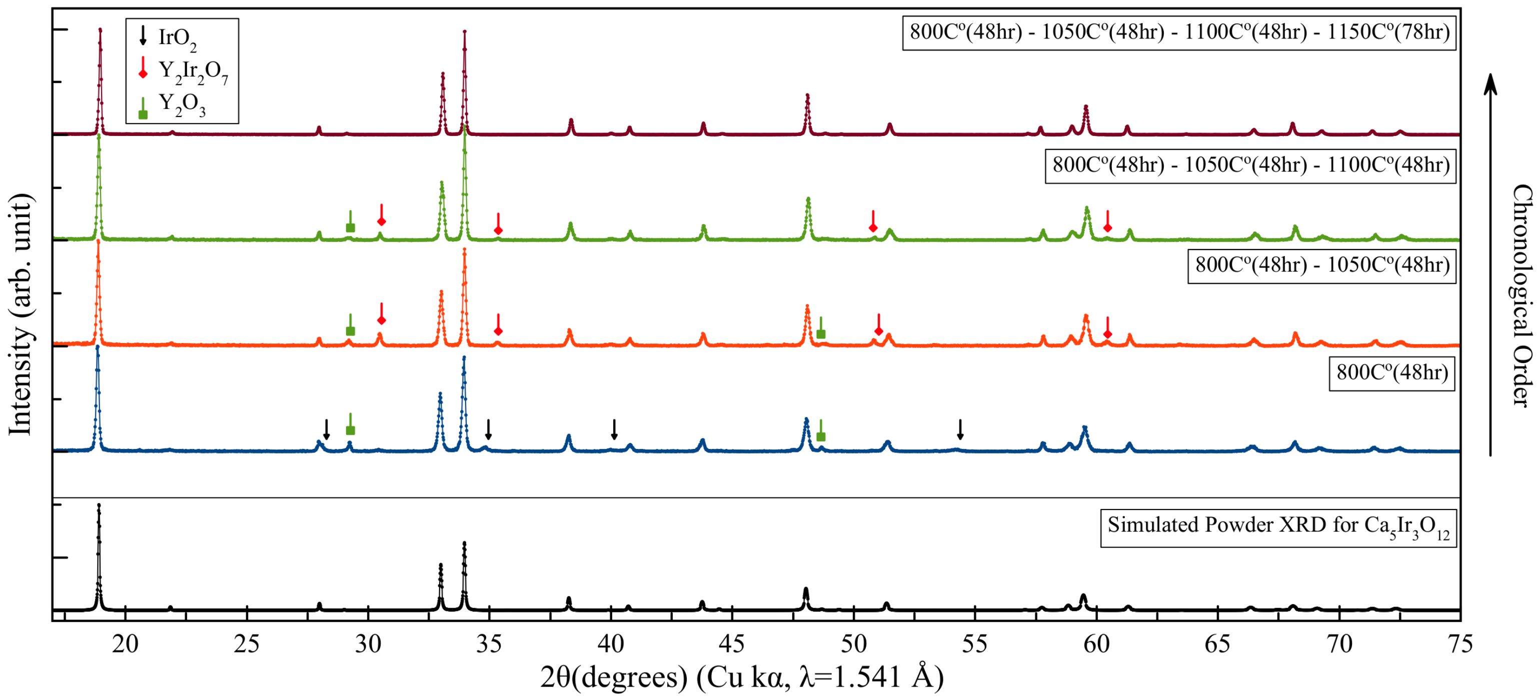

FIGURE 4.2: Temperature profile of a successful synthesis of $Ca_{5-x}Y_xIr_3O_{12}$ (nominal doping level: $x = 0.5$) in chronological order. The bottom panel displays a simulated powder XRD pattern for $Ca_5Ir_3O_{12}$ using $a = b = 9.42$Å, and $c = 3.19$Å as a comparison. Impurity phases are indicated by various arrow types.

refined lattice parameters for these samples are presented in Table 4.1. Figure 4.3 displays the powder XRD data for the final synthesized material, showing a noticeable shift in peak positions for (1,1,0) and (3,0,0) to larger values in 2θ, in agreement with the decreasing trend of the a and b lattice constants. Additionally, there is a shift in the peak position for (1,1,1) to the smaller values in 2θ, consistent with the increasing c lattice constant.

For the lower doping levels ($x = 0.25, 0.5, 1$), changes in lattice parameters were observed, and no impurity phases were detected. However, as shown in Figure 4.3, for the doping level of $x = 2$, it is impossible to eliminate the $Y_2Ir_2O_7$ impurity phase through additional regrinding and refiring at higher temperatures. Therefore, we conclude that the synthesis of polycrystals is only successful at lower doping levels. With the attempted nominal doping levels, the maximum doping level to obtain a phase-pure sample using this method is $x = 1$.

Nominal Doping Level	$a = b$ (Å)	c (Å)
$x = 0$	9.4062(5)	3.1876(1)
$x = 0.25$	9.3892(4)	3.1874(1)
$x = 0.5$	9.3780(4)	3.1890(1)
$x = 1$	9.3715(2)	3.2047(1)
$x = 2$	9.3578(3)	3.2103(1)

TABLE 4.1: Refined lattice parameters of $Ca_{5-x}Y_xIr_3O_{12}$ at nominal doping levels (x = 0.25, 0.5, 1, 2).

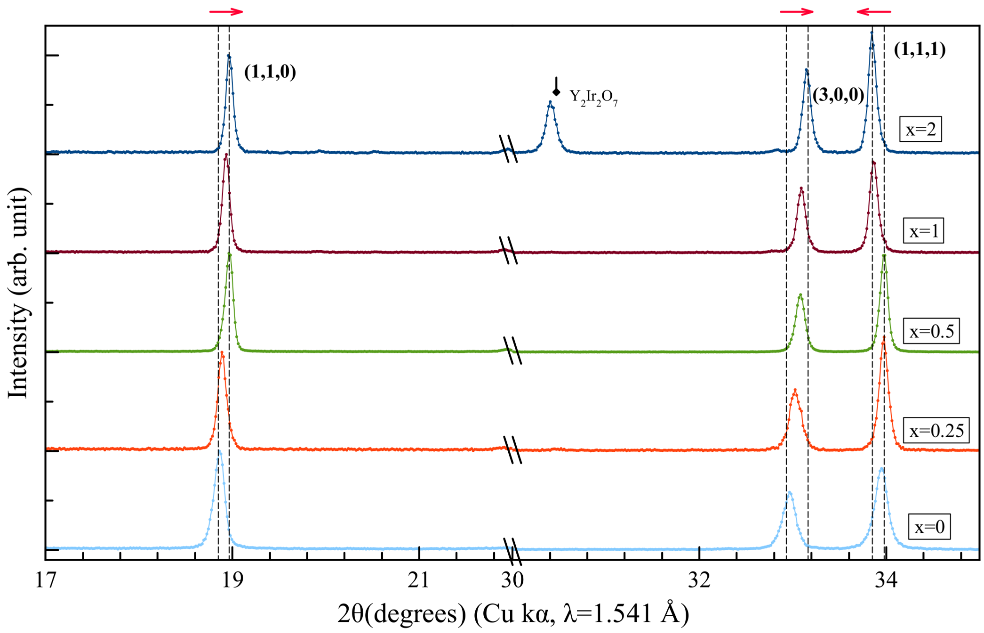

FIGURE 4.3: Powder XRD data for $Ca_{5-x}Y_xIr_3O_{12}$ at different nominal doping levels ($x = 0.25, 0.5, 1, 2$) with zoomed-in views of the (1,1,1), (1,1,0), and (3,0,0) diffraction peaks.

4.2.2 Synthesis and Phase Identification of Single Crystal Samples

Two methods were used for the synthesis of $Ca_{5-x}Y_xIr_3O_{12}$. In Method 1, stoichiometric amounts of $CaCO_3$, Ir metal or IrO_2, and annealed Y_2O_3 were used as starting materials. Additionally, $CaCl_2$ was added as a flux in a 1:5 sample-to-flux mass ratio. The starting material powder was mixed thoroughly and sealed in a platinum crucible, then fired in a box furnace to 1330°C for 4 hours. Then, it was cooled to 1150°C at a rate of 2°C/h, followed by further cooling to room temperature at 100°C/h.

For Method 1, several nominal doping levels were attempted. In the successful synthesis, after dissolving the flux in ethanol and removing powder impurities, rod-shaped single crystals with a hexagonal cross-section were obtained. A few rod-like crystals were ground for powder XRD analysis to investigate the crystalline structure. However, the detailed refinement of the powder XRD data was challenging due to the preferred orientation. Despite this, the observed shifts in peak position indicated changes in lattice parameters, consistent with the incorporation of Y^{3+} ions into the structure. Notably, three nominal doping levels, $x = 1, 2$, and 2.2, resulted in phase pure samples. Interestingly, the powder XRD results exhibited the same change in lattice constants for all three doping levels, suggesting that the actual doping level for these samples may be the same. The unsuccessful attempts at other nominal doping levels resulted in phase separation of doping levels or the formation of Ca_4IrO_6 as the dominant phase in single crystal form.

Method 2 involved an alternative approach to achieve different doping levels through single crystal growth. Initially, phase-pure polycrystals were synthesized using the method described in the previous section, with $CaCl_2$ added as a flux in a 1:5 sample-to-flux mass ratio. The powder material was mixed and placed in a platinum crucible, then heated in the box furnace to 1200°C for 4 hours. Subsequently, it was cooled to 800°C at a rate of 3°C/h, followed by further cooling to room temperature at 100°C/h.

Various doping levels were attempted using Method 2, and the obtained samples were analyzed using powder XRD. In successful syntheses, after dissolving the flux in ethanol and removing powder impurities, single crystals were obtained. These crystals primarily exhibited a single needle-like or bundle of needles-like shape. Phase-pure samples were successfully obtained at nominal doping levels of $x = 0, 0.5$, and 1. The unsuccessful attempts at other nominal doping levels resulted in phase separation of doping levels or the formation of $Y_2Ir_2O_7$ as the dominant phase in polycrystalline form.

Figure 4.4 displays the crystals obtained from successful growths using both methods. The doping levels were refined using single crystal XRD data, as described in the next section. It was observed that for higher doping levels, crystals were more likely to adopt a rod-like shape rather than a needle-like shape. Additionally, lower doped crystals were on average longer (about 2-4 mm in length) compared to higher doped crystals (typically less than 1 mm), suggesting that as the doping level increases, the crystals may become structurally less quasi-one-dimensional.

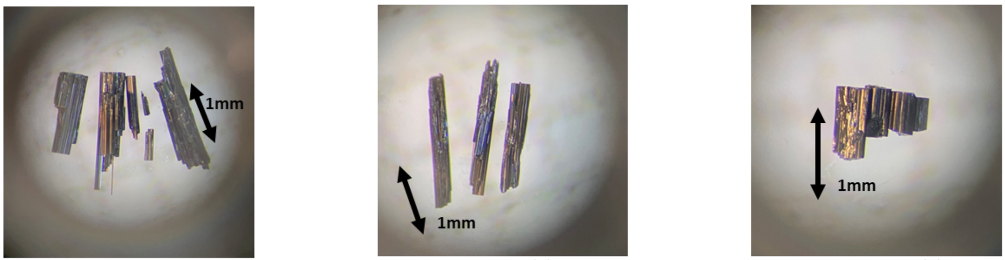

$x = 0$ Method 2 $x = 0.27(2)$ Method 2 $x = 0.65(2)$ Method 2

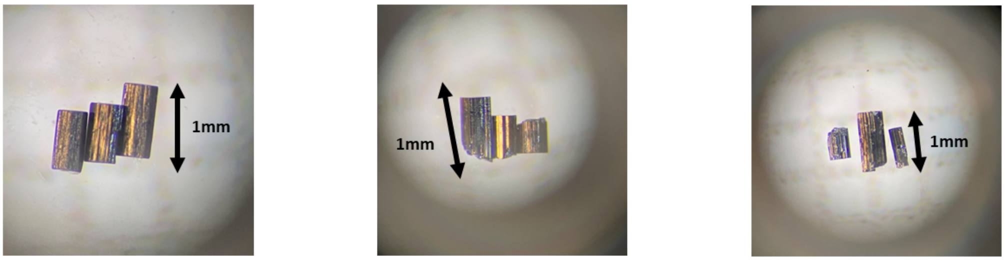

$x = 0.85(3)$ Method 2 $x = 1.43(1)$ Method 1 $x = 1.52(2)$ Method 1

FIGURE 4.4: Images of crystals under an optical microscope showing $Ca_{5-x}Y_xIr_3O_{12}$ synthesized using each method at various refined doping levels.

4.2.3 Structural Characterization of Single Crystal Samples

For further structural investigation, one crystal was selected from each growth batch, crushed into smaller pieces, and an approximately 40 × 40 × 40 micron sized piece was used for single crystal X-ray diffraction analysis. This detailed structural analysis aimed to determine the unit cell parameters, crystallographic data, and refine the doping levels of crystals from each growth. The selected refinement results are summarized in Tables 4.2, 4.3, and 4.4.

First, it is worth noting that the crystal structure remains largely unchanged with variations in doping levels. All doped samples retain the same $P\bar{6}2m$ space group as the parent compound. Atomic positions display no significant dependence on doping, and the general coordinates are provided in Table 4.3. Second, the determination of the doping level for each sample involves placing calcium and yttrium on the same 2d and 3g sites and refining the atomic occupancy. The total occupancy on each site was fixed at 1 and the ratio of each atom was refined. The results, as shown in Table 4.2, reveal that the refined doping levels are generally lower than the nominal doping levels. This observation aligns with the observation of non-rod or needle-like impurity single crystals and the presence of impurity powders at the bottom of the crucible. These findings explain the discrepancy between nominal and actual doping levels. Third, as presented in Table 4.2, a consistent trend emerges, wherein lattice parameters *a* and *b* decrease while *c* increases with increasing doping levels. This trend is consistent with the refinement results obtained from the polycrystalline XRD measurements. Together, these three observations confirm the successful incorporation of yttrium dopant into the structure. However, none of the crystals reached the targeted doping level of $x = 2$.

Nominal Doping Level (Method Used)	**Refined Doping Level**	**Refined Ir Oxidation State**	**a = b (Å)**	**c (Å)**
$x = 0$ (Method 2)	$x = 0$	+4.67	9.4213(6)	3.1958(5)
$x = 0.5$ (Method 2)	$x = 0.27(2)$	+4.58(1)	9.4079(10)	3.1962(3)
$x = 1$ (Method 2)	$x = 0.65(2)$	+4.45(1)	9.3824(14)	3.1948(8)
$x = 1$ (Method 2)	$x = 0.85(3)$	+4.83(2)	9.3941(6)	3.2008(3)
$x = 2$ (Method 1)	$x = 1.43(1)$	+4.19(1)	9.3617(6)	3.2119(3)
$x = 1$ (Method 1)	$x = 1.52(2)$	+4.16(1)	9.3615(11)	3.2140(5)

Table 4.2: Summary of refinement results for $Ca_{5-x}Y_xIr_3O_{12}$ at different nominal doping levels. Refined doping levels and lattice parameters demonstrate the successful doping.

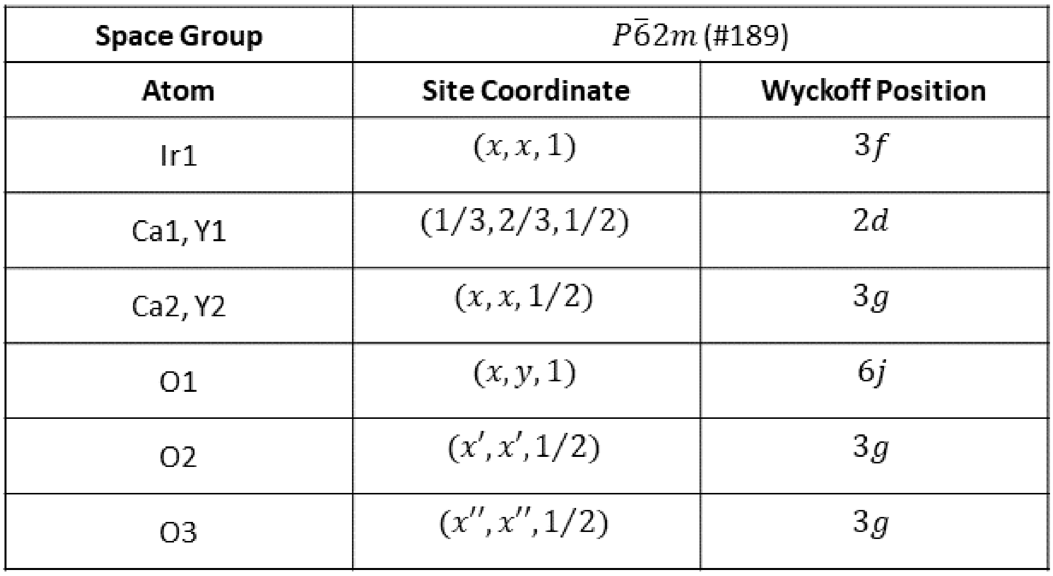

Space Group	$P\bar{6}2m$ (#189)	
Atom	**Site Coordinate**	**Wyckoff Position**
Ir1	$(x, x, 1)$	$3f$
Ca1, Y1	$(1/3, 2/3, 1/2)$	$2d$
Ca2, Y2	$(x, x, 1/2)$	$3g$
O1	$(x, y, 1)$	$6j$
O2	$(x', x', 1/2)$	$3g$
O3	$(x'', x'', 1/2)$	$3g$

Table 4.3: Summary of symmetry and crystallographic coordinates common to all measured $Ca_{5-x}Y_xIr_3O_{12}$ samples. Wyckoff positions represent special positions in the unit cell associated with the crystal structure's space group.

Next, we can examine structural parameters in Table 4.4 along with the graphic visualization of IrO_6 octahedra chains with atom labels depicted in Figure 4.5. First, the bond lengths between Ir and the surrounding six O atoms show a slight increase with doping, particularly noticeable in the Ir1-O1 bond length. This change leads to a more symmetrical local environment around the Ir site, resulting in reduced variation among the three non-equivalent Ir-O bond lengths within each IrO_6 octahedron. Second, the bond angle between O1-Ir1-O1 approaches 180° with increasing doping levels, indicating reduced distortion in the IrO_6 octahedron. These two results are important as they suggest the presence of an octahedral crystal electric field in the yttrium-doped samples, and these compound are likely to show $J_{\text{eff}} = 1/2$ physics if they have strong spin-orbit coupling, which is one of the criteria for realizing the Kitaev interaction. Third, the Ir1-O2-Ir1 bond angle remains at approximately 105^o, while the Ir1-O3-Ir1 bond angle remains at approximately 103^o as a function of doping. Importantly, these angles exhibit a significant deviation from the ideal 90^o bond angles required for the second criterion for realizing pure Kitaev interaction. The deviation in the two Ir-O-Ir bond angles suggest a Kitaev interaction with a significant Heisenberg interaction may be present along the edge-sharing IrO_6 octahedra chains.

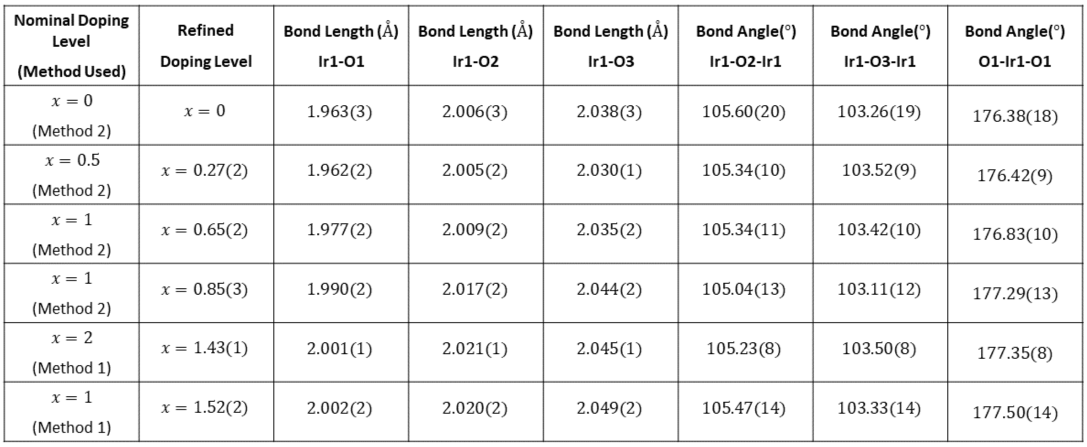

Nominal Doping Level (Method Used)	**Refined Doping Level**	**Bond Length (Å) Ir1-O1**	**Bond Length (Å) Ir1-O2**	**Bond Length (Å) Ir1-O3**	**Bond Angle(°) Ir1-O2-Ir1**	**Bond Angle(°) Ir1-O3-Ir1**	**Bond Angle(°) O1-Ir1-O1**
$x = 0$ (Method 2)	$x = 0$	1.963(3)	2.006(3)	2.038(3)	105.60(20)	103.26(19)	176.38(18)
$x = 0.5$ (Method 2)	$x = 0.27(2)$	1.962(2)	2.005(2)	2.030(1)	105.34(10)	103.52(9)	176.42(9)
$x = 1$ (Method 2)	$x = 0.65(2)$	1.977(2)	2.009(2)	2.035(2)	105.34(11)	103.42(10)	176.83(10)
$x = 1$ (Method 2)	$x = 0.85(3)$	1.990(2)	2.017(2)	2.044(2)	105.04(13)	103.11(12)	177.29(13)
$x = 2$ (Method 1)	$x = 1.43(1)$	2.001(1)	2.021(1)	2.045(1)	105.23(8)	103.50(8)	177.35(8)
$x = 1$ (Method 1)	$x = 1.52(2)$	2.002(2)	2.020(2)	2.049(2)	105.47(14)	103.33(14)	177.50(14)

TABLE 4.4: Summary of refinement results for $Ca_{5-x}Y_xIr_3O_{12}$ at different nominal and refined doping levels. Three bond lengths and three bond angles of interest are listed. Atom labels used correspond to positions listed in Table 4.3, and are graphically shown in Figure 4.5.

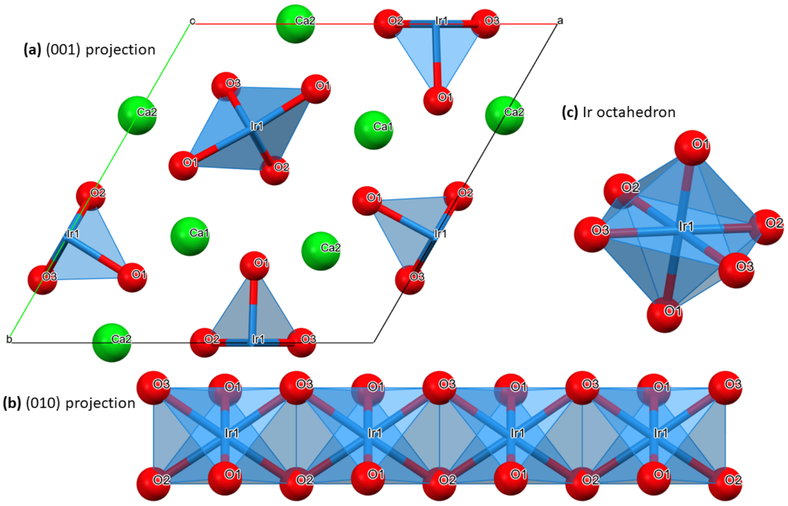

FIGURE 4.5: Visualization of $Ca_{5-x}Y_xIr_3O_{12}$ crystal structure in Ball-and-stick representation. (a) (001) projection from the single crystal X-ray diffraction refinement of the undoped sample. (b) (010) projection illustrating an IrO_6 octahedra chain with atom labels. (c) IrO_6 octahedron with with atom labels.

In summary, the refined crystal structures confirm the successful incorporation of yttrium into the parent compound, as evidenced by changes in lattice parameters, bond lengths, and bond angles. However, it is important to note that the $Ca_{5-x}Y_xIr_3O_{12}$ structure still exhibits notable deviations from the ideal mechanism proposed by G. Jackeli and G. Khaliullin for realizing the Kitaev interaction. While the bond lengths indicate a more symmetrical local environment around iridium as a function of doping, the two Ir-O-Ir bond angles suggest a distortion in each IrO_6 octahedron. Furthermore, it is worth noting that the targeted doping level of $x = 2$ for achieving a pure Ir^{4+} $J_{\text{eff}} = 1/2$ system was not achieved through the attempted single crystal synthesis. Nevertheless, the investigation of $Ca_{5-x}Y_xIr_3O_{12}$ samples remains interesting, as the highest doping level achieved ($x = 1.52$ or approximately 30% doping) is considerably higher than any previously studied doped $Ca_5Ir_3O_{12}$ system. Therefore, a detailed study of the electronic and magnetic properties was conducted as a function of doping level.

4.3 Electronic State Characterization

High Energy Resolution Fluorescence Detected X-ray Absorption Spectroscopy (HERFD-XAS) measurements were conducted on $Ca_{5-x}Y_xIr_3O_{12}$ samples at both the Ir L_3 and L_2 edges, following the methodology outlined in Chapter 2. The HERFD-XAS measurements provided insights into the electronic characteristics of the samples, and this section will focus on presenting results relevant to Ir valence, crystal electric field effects, and the strength of spin-orbit coupling.

First, XAS is used to probe Ir valence by examining the chemical shifts in the “white line" feature at both Ir L_3 and L_2 edges. The energy of this feature tends to increase with rising oxidation state, as more energy is required for ionization as the number of electrons around the positively charged nucleus is reduced. Figure 4.6 displays the X-ray absorption near edge structure (XANES) region of the XAS spectra. The red lines in Figure 4.6 serve as visual guides, showing the decrease in energy of the “white line" feature at both Ir L_3 and L_2 edges from the undoped sample (x=0 with $Ir^{4.67+}$) to the maximally doped sample (x=1.52(2) with $Ir^{4.16(1)+}$). This shift to lower energy indicates a decrease in oxidation states with increasing doping, consistent with the refined doping level and oxidation state determined from single crystal XRD results. However, it is important to note that the resolution of the XAS data prevents clear distinction of small changes in oxidation state. As a result, it becomes challenging to distinguish between similar doping levels (eg. $x = 0.65(2)$ and 0.85(3), or $x = 1.43(1)$ and 1.52(2)).

Similarly, Figure 4.7 offers a comparative view of the undoped and maximally doped samples in relation to Sr_2YIrO_6 and Sr_2IrO_4, representing Ir^{5+} and Ir^{4+} reference samples, respectively. Once more, the red lines in Figure 4.7 serve as visual guides, indicating the decrease in energy of the “white line" feature at both Ir L_3 and L_2 edges from the

Ir^{5+} reference to the Ir^{4+} reference sample. The undoped sample, x=0 with $\mathrm{Ir}^{4.67+}$ oxidation state, exhibits an energy slightly below that of the Ir^{5+} reference. Conversely, the maximally doped sample, x=1.52(2) with $\mathrm{Ir}^{4.16(1)+}$ oxidation state, displays an energy very close to the Ir^{4+} reference, indicating the successful doping of yttrium. In summary, the XAS results reveals the possibility of determining changes in oxidation states through shifts in the "white-line" energy within the Ir L_3 and L_2 edges, as a function of doping. However, due to the resolution limitations of XAS, precise quantification of the oxidation state in the doped samples is challenging.

Second, it is noteworthy that in both Figures 4.6 and 4.7, the Ir L_3 edge XANES spectrum of the measured samples shows two peaks, while the Ir L_2 edge XANES spectrum has only one peak. This difference arises because the Ir L_3 edge involves electron transitions from $2p_{3/2}$ to both $5d_{3/2}$ (primarily t_{2g} in character) and $5d_{5/2}$ (primarily e_g in character) orbitals. Consequently, the Ir L_3 edge XANES spectrum can be used to probe the total number of holes in all 5d orbitals. With the energy resolution of HERFD-XAS, it becomes possible to detect the splitting between the e_g and t_{2g} states from the Ir L_3 edge XANES spectrum. In this context, the lower energy peak corresponds to the t_{2g} states, while the higher energy peak corresponds to the e_g states. The strength of the crystal electric field splitting (denoted as 10Dq) can be quantified by subtracting the energies $E_{L3_{t2g}}$ from $E_{L3_{eg}}$. The results, presented in Table 4.5, indicate that within the fitting uncertainty, there is no significant change in the strength of the crystal electric field splitting as a function of doping.

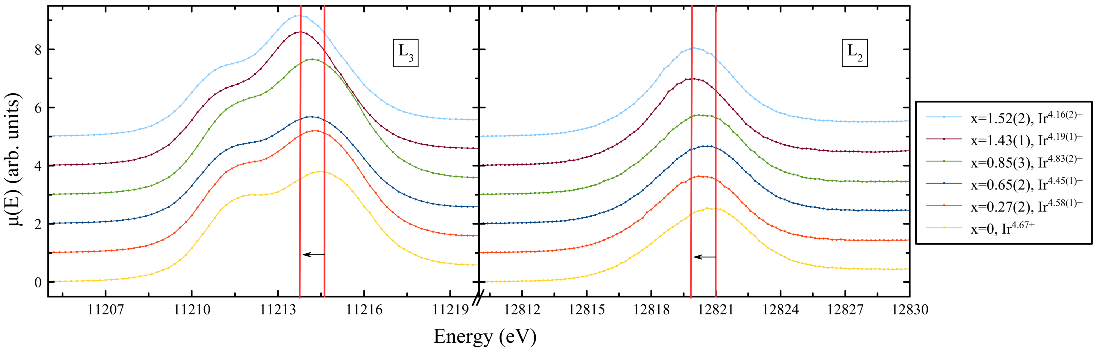

FIGURE 4.6: XANES region for $Ca_{5-x}Y_xIr_3O_{12}$ at the Ir L_3 (left) and L_2 (right) edge. The energy of the "white line" feature decreases as the doping level increases. This chemical shift indicat a steady decrease in oxidation state. The red lines serve as visual guides, showing the decrease in energy of the "white line" from the undoped sample (x=0 with $Ir^{4.67+}$) to the maximally doped sample (x=1.52(2) with $Ir^{4.16(1)+}$).

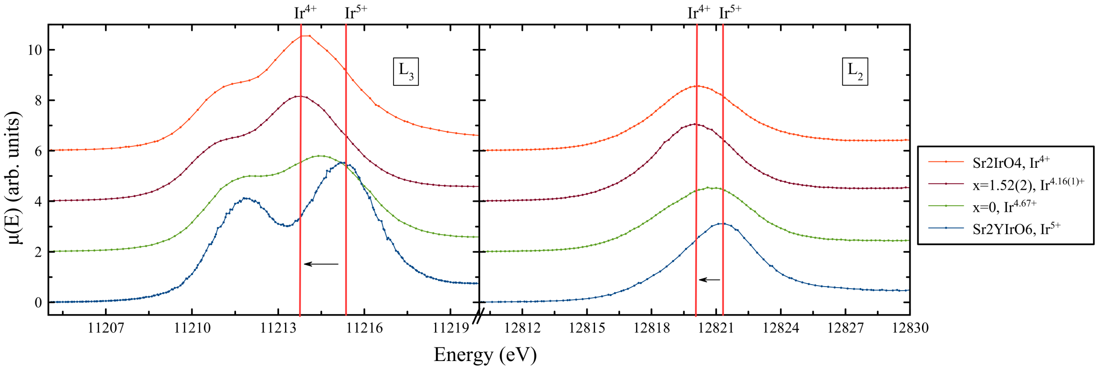

FIGURE 4.7: XANES region for $Ca_{5-x}Y_xIr_3O_{12}$ at $x = 0$ and $x = 1.52(2)$ compared to Sr_2YIrO_6 (Ir^{5+}) and Sr_2IrO_4 (Ir^{+4}) reference at Ir L_3 and L_2 edges. The red lines serve as visual guides, indicating the decrease in energy of the "white line" feature from the Ir^{5+} reference to the Ir^{4+} reference sample.

Third, the branching ratio can be extracted from the ratio of integrated intensity of the "white line" feature at the Ir L_3 and L_2 edges ($BR = I_{L3}/I_{L2}$). As shown in Equations 2.4.1 in Chapter 2, assuming negligible spin-orbit coupling (SOC), the BR is anticipated to be 2. Table 4.5 shows the calculated BR from fitted experimental data for $\text{Ca}_{5-x}\text{Y}_x\text{Ir}_3\text{O}_{12}$ samples all exceed 2, indicating nonzero SOC effect. However, no significant trend was observed as the function the doping levels. Similarly, the strength of spin-orbit coupling ($\langle L \cdot S \rangle$) can also be estimated using Equation 2.4.2 in Chapter 2. The result displayed in Table 4.5 shows a non-zero $\langle L \cdot S \rangle$ for all $\text{Ca}_{5-x}\text{Y}_x\text{Ir}_3\text{O}_{12}$ samples, however no obvious trend was observed as the function the doping levels. Furthermore, all $\text{Ca}_{5-x}\text{Y}_x\text{Ir}_3\text{O}_{12}$ samples show a comparable magnitude of BR and $\langle L \cdot S \rangle$ to the canonical $J_{\text{eff}} = 1/2$ system Sr_2IrO_4. This suggest large SOC effect in all $\text{Ca}_{5-x}\text{Y}_x\text{Ir}_3\text{O}_{12}$ samples, which is one signature of $J_{\text{eff}} = 1/2$ system.

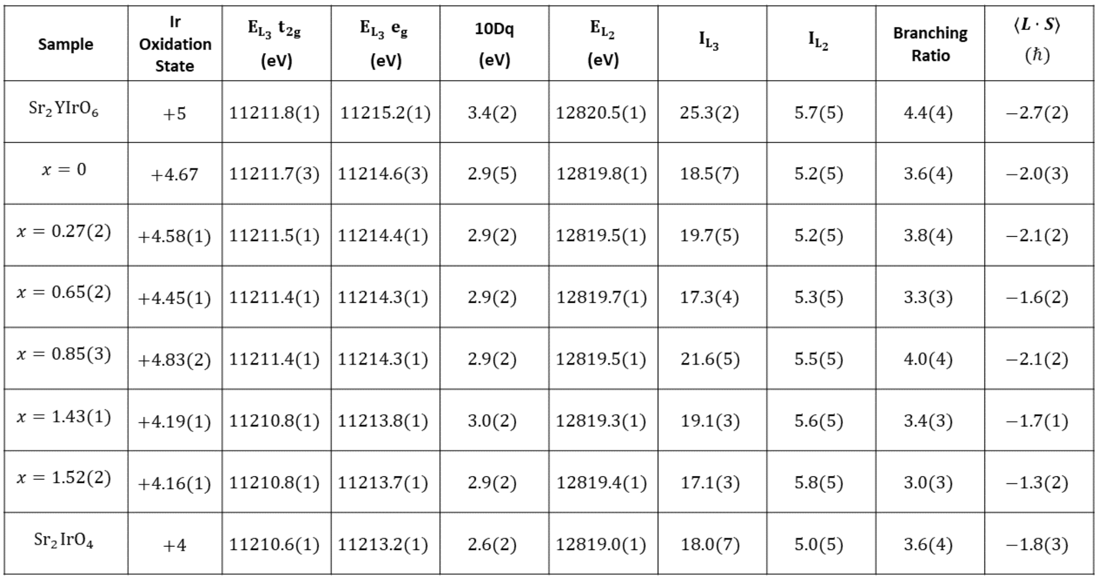

Sample	Ir Oxidation State	E_{L_3} t_{2g} (eV)	E_{L_3} e_g (eV)	10Dq (eV)	E_{L_2} (eV)	I_{L_3}	I_{L_2}	Branching Ratio	$\langle L \cdot S \rangle$ ($\hbar$)
Sr_2YIrO_6	+5	11211.8(1)	11215.2(1)	3.4(2)	12820.5(1)	25.3(2)	5.7(5)	4.4(4)	−2.7(2)
$x = 0$	+4.67	11211.7(3)	11214.6(3)	2.9(5)	12819.8(1)	18.5(7)	5.2(5)	3.6(4)	−2.0(3)
$x = 0.27(2)$	+4.58(1)	11211.5(1)	11214.4(1)	2.9(2)	12819.5(1)	19.7(5)	5.2(5)	3.8(4)	−2.1(2)
$x = 0.65(2)$	+4.45(1)	11211.4(1)	11214.3(1)	2.9(2)	12819.7(1)	17.3(4)	5.3(5)	3.3(3)	−1.6(2)
$x = 0.85(3)$	+4.83(2)	11211.4(1)	11214.3(1)	2.9(2)	12819.5(1)	21.6(5)	5.5(5)	4.0(4)	−2.1(2)
$x = 1.43(1)$	+4.19(1)	11210.8(1)	11213.8(1)	3.0(2)	12819.3(1)	19.1(3)	5.6(5)	3.4(3)	−1.7(1)
$x = 1.52(2)$	+4.16(1)	11210.8(1)	11213.7(1)	2.9(2)	12819.4(1)	17.1(3)	5.8(5)	3.0(3)	−1.3(2)
Sr_2IrO_4	+4	11210.6(1)	11213.2(1)	2.6(2)	12819.0(1)	18.0(7)	5.0(5)	3.6(4)	−1.8(3)

TABLE 4.5: Summary of HERFD-XAS measurements conducted on $Ca_{5-x}Y_xIr_3O_{12}$ samples at various refined doping levels, including Sr_2IrO_4 (Ir^{4+}) and Sr_2YIrO_6 (Ir^{5+}) reference samples. Peak positions of the "white line" feature ($E_{L3_{t2g}}$, $E_{L3_{eg}}$, and E_{L2}) are determined using Gaussian fits with an arctangent function applied to Ir L_3 and L_2 edge spectra, with uncertainties derived from the fit function. $10Dq$ crystal field splitting is calclated using $E_{L3_{t2g}}$ and $E_{L3_{eg}}$ peak positions. The intensity of the "white line" features in Ir L_2 and L_3 edges is quantified through numerical integration, with uncertainties obtained by fitting the same spectrum with different normalization regions using ATHENA. The branching ratio (BR) and the spin-orbit expectation ($\langle L \cdot S \rangle$) are calculated based on the fitted data.

In summary, the HERFD-XAS results show a consistent decrease in oxidation states as a function of doping, as evidenced by noticeable chemical shifts in both Ir L_2 and L_3 spectra. Additionally, the characteristic two-peak line shape observed at the L_3 edge in all samples is indicative of crystal electric field effects. Furthermore, these results indicate the existence of a strong spin-orbit coupling effect, as inferred from the calculated branching ratio and spin-orbit expectation value. Notably, there is no apparent doping dependence observed in 10Dq, branching ratio, or the spin-orbit expectation value. These findings suggest that $Ca_{5-x}Y_xIr_3O_{12}$ samples could potentially exhibit $J_{\text{eff}} = 1/2$ ground states due to the strong spin-orbit coupling within an octahedral crystal electric field.

4.4 Magnetic Characterization

Magnetic susceptibility measurements were conducted on the $Ca_{5-x}Y_xIr_3O_{12}$ samples with a SQUID magnetometer using the method described in Chapter 2. Figure 4.8 displays the experimental results, which includes zero field cooled (ZFC) and field cooled (FC) susceptibility measurements for all $Ca_{5-x}Y_xIr_3O_{12}$ samples. These measurements were performed under an applied magnetic field of 1000Oe, with the field oriented perpendicular and parallel to the c-axis of the crystals, or the IrO_6 edge-sharing octahedral chain. Figure 4.9 provides Curie-Weiss fits within the paramagnetic regime (150-300K), based on the inverse zero field cooled susceptibility data. Table 4.6 summarizes both the observed features, including the transition temperature (T_N) and ZFC-FC hysteresis temperature (T_H), as well as the fitted results, which include Curie-Weiss temperature (T_{CW}), net effective moment (μ_{eff}), and frustration index (f). Based on the susceptibility results, the samples can be categorized into three groups: no doping (x=0), low doping levels (x=0.27(2), 0.65(2), 0.85(3)), and high doping levels (x=1.43(1), 1.52(2)).

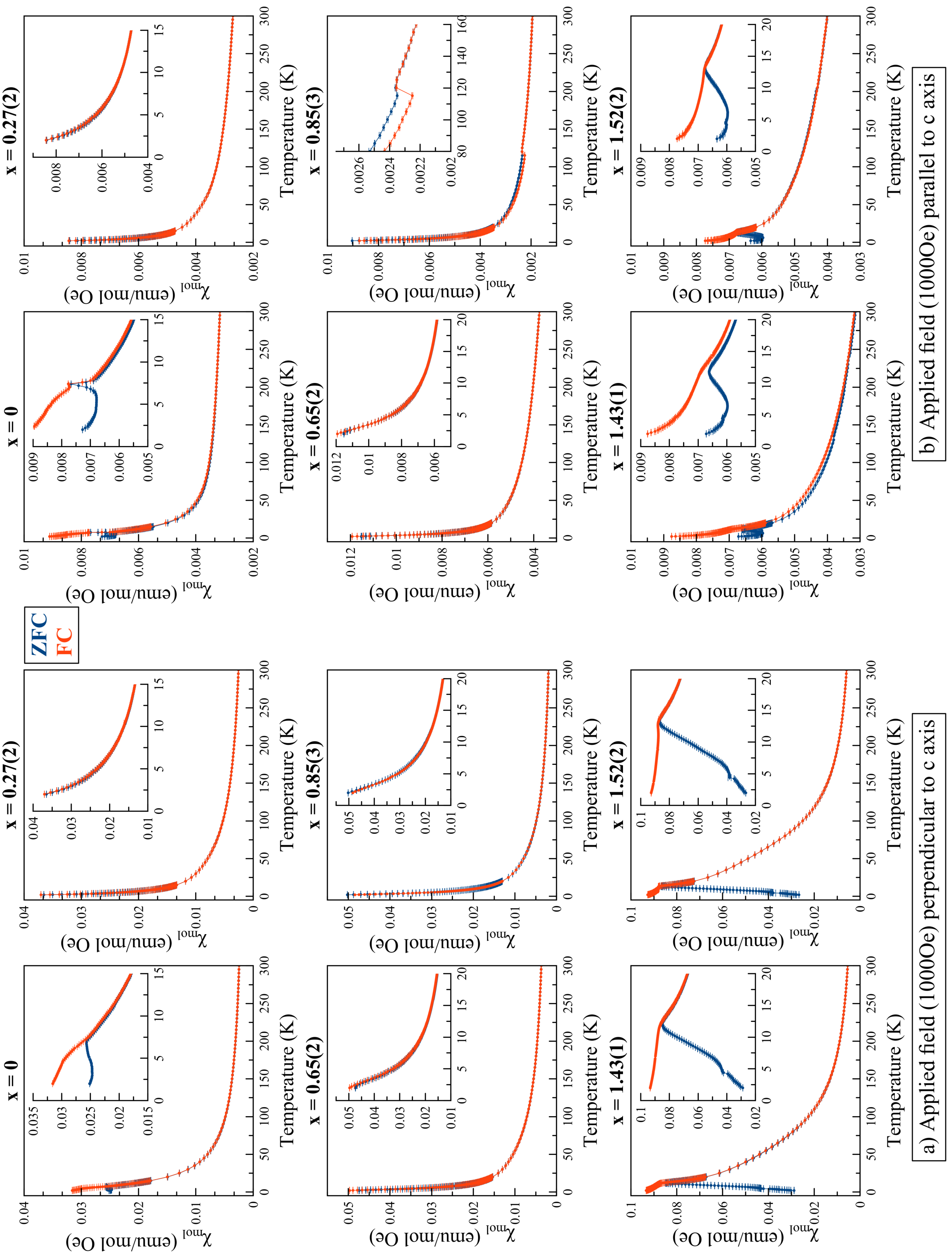

a) Applied field (1000Oe) perpendicular to c axis

b) Applied field (1000Oe) parallel to c axis

FIGURE 4.8: Zero field cooled (ZFC) and field cooled (FC) susceptibilities of $Ca_{5-x}Y_xIr_3O_{12}$ single crystal at various doping levels under an applied field of B=1000Oe. a) susceptibility data with field perpendicular to c axis. b) susceptibility data with field parallel to c axis.

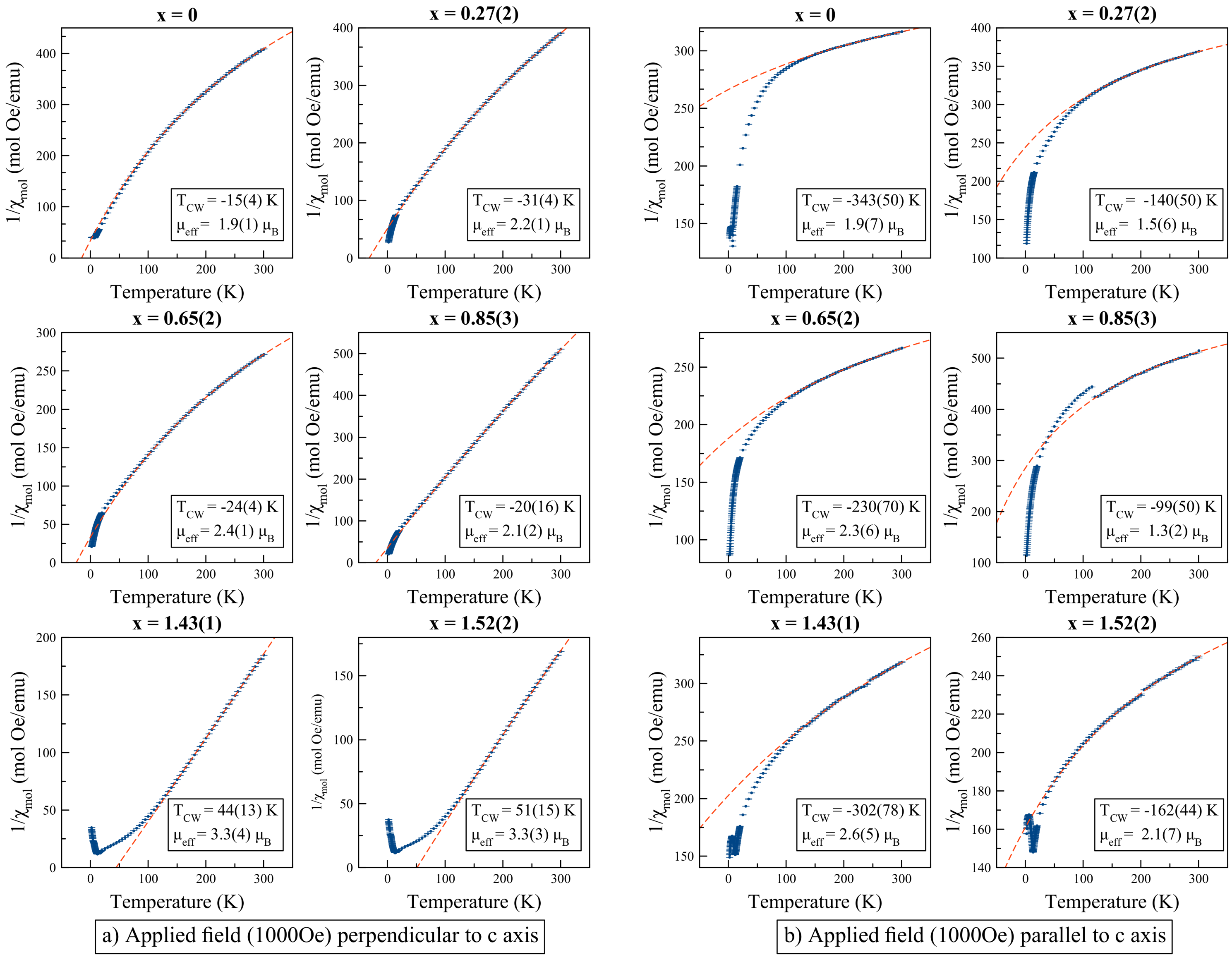

a) Applied field (1000Oe) perpendicular to c axis

b) Applied field (1000Oe) parallel to c axis

FIGURE 4.9: The inverse ZFC susceptibility plots for $Ca_{5-x}Y_xIr_3O_{12}$ single crystal at various doping levels with a Curie-Weiss fit with a temperature-independent term in red. The Curie-Weiss temperature and effective moment is determined by fitting temperature region above 150K. a) inverse ZFC susceptibility data with field perpendicular to c axis. b) inverse ZFC susceptibility data with field parallel to c axis.

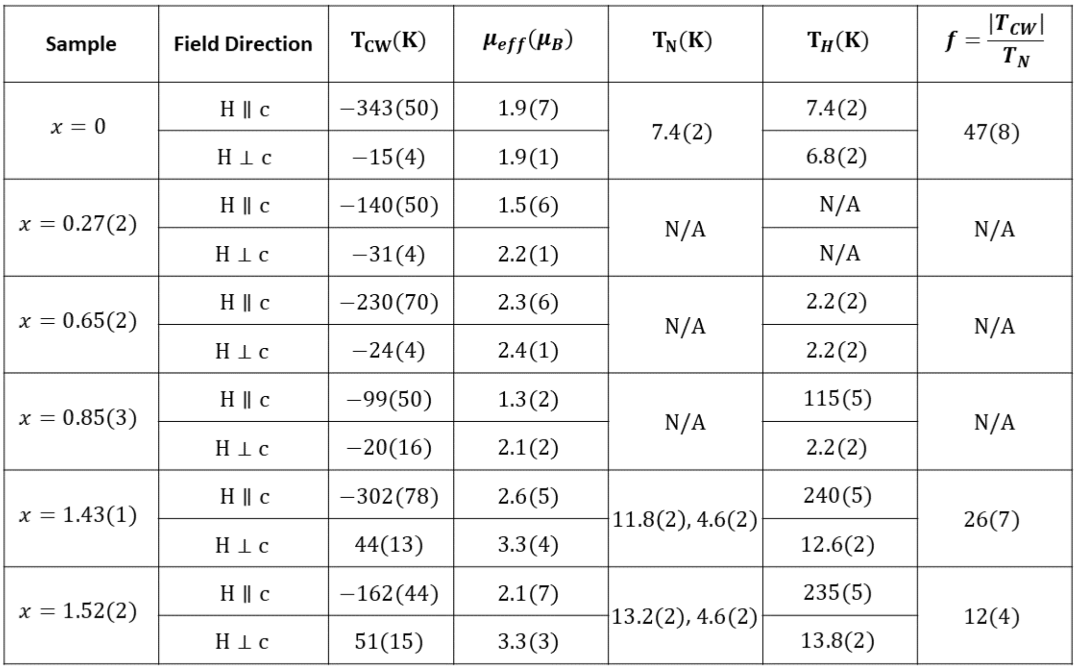

Sample	**Field Direction**	$\mathbf{T_{CW}(K)}$	$\mu_{eff}(\mu_B)$	$\mathbf{T_N(K)}$	$\mathbf{T_H(K)}$	$f = \frac{\lvert T_{CW} \rvert}{T_N}$
$x = 0$	H ∥ c	−343(50)	1.9(7)	7.4(2)	7.4(2)	47(8)
	H ⊥ c	−15(4)	1.9(1)		6.8(2)	
$x = 0.27(2)$	H ∥ c	−140(50)	1.5(6)	N/A	N/A	N/A
	H ⊥ c	−31(4)	2.2(1)		N/A	
$x = 0.65(2)$	H ∥ c	−230(70)	2.3(6)	N/A	2.2(2)	N/A
	H ⊥ c	−24(4)	2.4(1)		2.2(2)	
$x = 0.85(3)$	H ∥ c	−99(50)	1.3(2)	N/A	115(5)	N/A
	H ⊥ c	−20(16)	2.1(2)		2.2(2)	
$x = 1.43(1)$	H ∥ c	−302(78)	2.6(5)	11.8(2), 4.6(2)	240(5)	26(7)
	H ⊥ c	44(13)	3.3(4)		12.6(2)	
$x = 1.52(2)$	H ∥ c	−162(44)	2.1(7)	13.2(2), 4.6(2)	235(5)	12(4)
	H ⊥ c	51(15)	3.3(3)		13.8(2)	

Table 4.6: Summary table of the susceptibility results for each doping level in two field directions. The table includes the observed antiferromagnetic transition temperature (T_N), the ZFC and FC splitting temperature (T_H), as well as the fitted Curie-Weiss temperature (T_{CW}), estimated effective moment (μ_{eff}), and frustration index (f). f is calculated using the maximum Curie-Weiss temperature of the sample.

In the undoped case ($x = 0$), several observations can be made. First, in the field parallel to the c-axis, there is a sharp anomaly in the susceptibility curve at $T_N = 7.4(2)K$, indicating a phase transition to antiferromagnetic ordering below T_N, which is consistent with previous reports [40][39]. In the field perpendicular to the c-axis, the susceptibility shows a weak anomaly at the same T_N. Second, in both field directions, the ZFC and FC curves diverge below T_N, which suggests the presence of magnetic domains that align with the applied field. Consequently, the FC magnetic susceptibility is larger below T_N compared to the ZFC susceptibility. Third, the negative T_{CW} values determined through the Curie-Weiss fit indicate a net antiferromagnetic interaction in both field directions. However, the antiferromagnetic interaction is more dominant in the parallel field direction, as indicated by the strength of the interaction, represented by the magnitude of T_{CW}, which is larger compared to the perpendicular field direction.

In the low doping levels (5-20%) where $x = 0.27(2), 0.65(2)$, and $0.85(3)$, different observations can be seen compared to the undoped sample. First, the 7.5K antiferromagnetic transition observed in the undoped sample ($x = 0$) is completely suppressed in both field directions, and no anomalies are observed in the susceptibility curves. Second, despite the absence of the magnetic phase transition, the negative T_{CW} values indicate the presence of a net antiferromagnetic interaction in both field directions. Similar to the undoped case, the parallel field direction exhibits a larger magnitude of T_{CW} than the perpendicular direction, suggesting that the dominant net antiferromagnetic interaction is along the chain direction. Third, small ZFC and FC splitting emerges around 2.2K in these samples, indicating a glassy behavior. However, an exception is observed in the case of $x = 0.85(3)$ under parallel field direction, where a ZFC and FC splitting occurs around 120K. This distinctive high-temperature feature is reproducible in lower field (B=100Oe) measurement, and with a temperature increment of 1K, it becomes evident that this transition is smooth and intrinsic to the sample. Nevertheless, the origin of this feature remains unclear. One potential explanation is a minor contamination of $Y_2Ir_2O_7$ in the sample, as it was reported to exhibit an enlargement of ZFC and FC splitting below the bifurcation temperature at 130K [51].

In the high doping levels (25-30%) where $x = 1.43(1), 1.52(2)$, new magnetic transitions emerge. First, two distinct magnetic transitions occur. A noticeable cusp appears in the ZFC curve at $T_{N1} = 11.8(2)$ for $x = 1.43(1)$ and at $T_{N1} = 13.2(2)$ for $x = 1.52(2)$. Determining the exact magnetic ground states associated with this transition requires additional characterization using other techniques. Additionally, a minor anomaly emerges at $T_{N2} = 4.6(2)$ for both samples. This anomaly is likely an artifact caused by ZFC and FC irreversibility during warming up through the boiling point of liquid Helium-4. Notably, the transition around T_{N1} exhibits more pronounced characteristics when the magnetic field is oriented perpendicular to the c-axis. Second, in the field parallel to the c-axis, a small ZFC and FC splitting occurs at a higher temperature (240(5) K) and becomes more significant below T_{N1}. Similarly, in the field perpendicular to the c-axis, a substantial ZFC and FC splitting occurs below T_{N1}, providing evidence of potential spin glass behavior below the transition temperature. Third, a large negative T_{CW} value in the field along the c-axis points to a net antiferromagnetic interaction along the chain direction. Conversely, a small positive T_{CW} value in the field perpendicular to the c-axis suggests a small net ferromagnetic interaction in the in-plane direction. This might indicate the presence of canted antiferromagnetic ordering along the c-axis, which, in turn, leads to a small ferromagnetic in-plane component below T_{N1}.

In summary, the magnetic susceptibility results show interesting trends as the doping level varies in $Ca_{5-x}Y_xIr_3O_{12}$ samples. When the doping level increases to the range of 5-20%, the previously observed magnetic transition at $T_N = 7.4(2)$K completely vanishes. Upon further doping to 25-30%, a new magnetic transition emerges at $T_{N1} = 11.8(2)$K, which becomes even more elevated at the highest doping level of $x = 1.52(2)$, reaching $T_{N1} = 13.2(2)$K. The Curie-Weiss temperatures (T_{CW}) obtained from our analysis suggest a dominant net antiferromagnetic interaction along the IrO_6 edge-sharing octahedral chain in all $Ca_{5-x}Y_xIr_3O_{12}$ samples. However, in the direction perpendicular to the chain, there is a transition from a small net antiferromagnetic interaction to a net ferromagnetic interaction at higher doping levels. The frustration indices in Table 4.6 suggest large magnetic frustration along the chain direction, possibly due to the presence of competing interactions in this direction. Furthermore, all $Ca_{5-x}Y_xIr_3O_{12}$ samples in Figure 4.8 show significant anisotropy in susceptibility between directions parallel ($\chi_{\|c}$) and perpendicular ($\chi_{\perp c}$) to the c-axis, as expected for low-dimensional systems. This anisotropy increases as function of doping. In the undoped sample, $\chi_{\perp c}$ is approximately three times greater than $\chi_{\parallel c}$, while in the highly doped samples, $\chi_{\perp c}$ is roughly ten times greater than $\chi_{\parallel c}$. Finally, based solely on susceptibility measurements, we can only speculate about the magnetic ground states of $Ca_{5-x}Y_xIr_3O_{12}$ samples. To conclusively identify the magnetic ground states below these transition temperatures, magnetic diffraction studies using neutrons or resonant X-rays are required.

4.5 Conclusion

In conclusion, our study has successfully confirmed the incorporation of yttrium into the $Ca_5Ir_3O_{12}$ structure through structural and electronic characterizations. The doping levels determined from single crystal XRD refinement align with the chemical shift of the "white line" feature observed in X-ray absorption spectroscopy results. Notably, the highest doping level achieved is $x = 1.52(2)$, resulted in an oxidation state of $Ir^{4.16+}$, indicating a mixed valence of Ir^{4+} and Ir^{5+} in a 5:1 ratio. Therefore, our original goal of achieving a doping level of $x = 2$ to attain a pure Ir^{4+} oxidation state for the realization of quasi-one-dimensional Kitaev chains was not met. The further electronic characterizations have revealed the presence of crystal electric field splitting and evidence of strong spin-orbit coupling in all synthesized $Ca_{5-x}Y_xIr_3O_{12}$ samples. Additionally, the magnetic characterizations showed the emergence of a new magnetic transitions with increasing doping levels, exchange frustration along the IrO_6 chain, and magnetic anisotropy. These intriguing electronic and magnetic behaviors open up many possibilities for further investigations for future research.

Chapter 5

Conclusion

The original objective of this project was to search for an experimental realization of the low-dimensional Kitaev chain, satisfying the two criteria outlined by G. Jackeli and G. Khaliullin. First, the chosen material should have a $J_{\text{eff}} = 1/2$ ground state, allowing the emergence of bond-dependent Kitaev interactions from strong spin-orbit coupling. Second, the material should contain a 90° metal-oxygen-metal (TM-O-TM) bond geometry, such as an edge-sharing octahedral crystal structure, in order to minimize the Heisenberg interaction and increase the chance of the experimental observation of the weak Kitaev interaction.

The first potential candidate we considered for the quasi-one-dimensional Kitaev chain that satisfies the two criteria is Ca_2IrO_4. However, our attempted synthesis and characterization revealed that this material cannot be synthesized under the reported conditions and methods. The structural and magnetic analyses showed the absence of calcium at the (0,0,0) position and an antiferromagnetic transition occurring around 7.4(5)K, which is consistent with the behavior of $Ca_5Ir_3O_{12}$. $Ca_5Ir_3O_{12}$ exhibits a mixed valence state of $Ir^{4.67+}$, with a Ir^{4+} (magnetic) to Ir^{5+} (non-magnetic) ratio of 1:2, instead of the ideal pure Ir^{4+} valence state in the Ca_2IrO_4 composition. Therefore, $Ca_5Ir_3O_{12}$ is not an ideal candidate due to the presence of non-magnetic Ir^{5+} along the chain.

Consequently, we need to explore an alternative approach for realizing the quasi-one-dimensional Kitaev chain. One potential solution is to tune the valence of the existing $Ca_5Ir_3O_{12}$ structure from $Ir^{4.67+}$ to Ir^{4+} through chemical doping. Yttrium emerged as a promising dopant, and we successfully incorporated yttrium into the $Ca_5Ir_3O_{12}$ structure, as confirmed by structural and electronic characterizations. However, the highest doping level achieved in this study was $x = 1.52(2)$, resulting in an oxidation state of $Ir^{4.16+}$ with Ir^{4+} to Ir^{5+} ratio of 5:1. Therefore, we did not meet our initial goal of achieving a doping level of $x = 2$ to attain a pure Ir^{4+} oxidation state for the realization of quasi-one-dimensional Kitaev chains. Additionally, structural characterization reveals that the TM-O-TM angles range from 105^o to 103^o, which significantly deviates from the ideal 90^o bond angle required for the realization of pure Kitaev interactions. Hence, additional interactions such as Heisenberg interactions should be considered.

Despite not achieving the pure Ir^{4+} oxidation state and not satisfying the ideal 90^o bond angle, $Ca_{5-x}Y_xIr_3O_{12}$ samples still exhibit interesting properties. First, the highest doping levels we reached are considerably higher than those in previously studied doped $Ca_5Ir_3O_{12}$. Second, electronic characterizations have revealed crystal electric field splitting and evidence of strong spin-orbit coupling in all synthesized $Ca_{5-x}Y_xIr_3O_{12}$ samples. Third, the magnetic susceptibility data shows that as the doping level increases, within the range of 5-20%, the magnetic transition around 7K observed in parent compound completely vanishes. Upon further doping to 25-30%, a new magnetic transition emerges at around 11-13K. The Curie-Weiss temperatures suggest the potential presence of canted antiferromagnetic ordering along the chain direction in the highly doped samples. The substantial ZFC and FC splitting might indicate potential ground states of a spin glass. However, further experimental investigation with different techniques is required to determine the exact magnetic ordering.

There are several possibilities for future research on $Ca_{5-x}Y_xIr_3O_{12}$ samples. First, in terms of searching for potential candidates for the quasi-one-dimensional Kitaev chain, we can consider using resonant inelastic X-ray scattering or inelastic neutron scattering to initially confirm if any of the synthesized $Ca_{5-x}Y_xIr_3O_{12}$ samples indeed exhibit a $J_{\text{eff}} = 1/2$ ground state. Subsequently, we can compare the experimental data with theoretical models to identify different types of interactions present in these $Ca_{5-x}Y_xIr_3O_{12}$ samples, ultimately confirming the presence of Kitaev interactions in these materials. Additionally, we can also explore other dopants. Ce^{4+} is another promising candidate, which can achieve a pure Ir^{4+} state with just $x = 1$ or 20% doping.

Second, regarding the study of the effect of chemical doping on $Ca_5Ir_3O_{12}$, further measurements, including heat capacity and resistivity, can be investigated as a function of doping. This investigation is particularly interesting to determine how the 105K anomaly in specific heat changes as function of doping. Furthermore, there have been no reports of neutron diffraction studies on the magnetic ordering vector and ordering parameter of $Ca_5Ir_3O_{12}$. Exploring how magnetic ordering vector and ordering parameter change as a function of doping will be interesting, as it also can help us understand the magnetic structure of $Ca_5Ir_3O_{12}$ and the nature of the new magnetic ordering that occurs in the highly doped samples. In conclusion, there is a lot of potential for further experimental investigations with $Ca_{5-x}Y_xIr_3O_{12}$ samples, and these studies may give surprising results.

Bibliography

[1] S. Trebst and C. Hickey, Physics Reports **950**, 1 (2022), ISSN 0370-1573, URL `https://www.sciencedirect.com/science/article/pii/S0370157321004051`.

[2] B. J. Kim, H. Jin, S. J. Moon, J.-Y. Kim, B.-G. Park, C. S. Leem, J. Yu, T. W. Noh, C. Kim, S.-J. Oh, et al., Phys. Rev. Lett. **101**, 076402 (2008), URL `https://link.aps.org/doi/10.1103/PhysRevLett.101.076402`.

[3] G. Jackeli and G. Khaliullin, Phys. Rev. Lett. **102**, 017205 (2009), URL `https://link.aps.org/doi/10.1103/PhysRevLett.102.017205`.

[4] A. Kitaev, Annals of Physics **321**, 2 (2006), ISSN 0003-4916, URL `https://www.sciencedirect.com/science/article/pii/S0003491605002381`.

[5] C. E. Agrapidis, J. van den Brink, and S. Nishimoto, Sci Rep **8**, 1815 (2018).

[6] N. F. Mott, *Metal-Insulator Transitions* (Taylor and Francis, London/Philadelphia, 1990).

[7] J. Hubbard, Proceedings of the Royal Society of London. Series A, Mathematical and Physical Sciences **276**, 238 (1963), URL `http://www.jstor.org/stable/2414761`.

[8] M. Imada, A. Fujimori, and Y. Tokura, Rev. Mod. Phys. **70**, 1039 (1998), URL `https://link.aps.org/doi/10.1103/RevModPhys.70.1039`.

[9] W. Witczak-Krempa, G. Chen, Y. B. Kim, and L. Balents, Annual Review of Condensed Matter Physics **5**, 57 (2014), URL `https://doi.org/10.1146/annurev-conmatphys-020911-125138`.

[10] K. I. Kugel' and D. I. Khomskiĭ, Soviet Physics Uspekhi **25**, 231 (1982), URL `https://dx.doi.org/10.1070/PU1982v025n04ABEH004537`.

[11] J. Wen, S. Yu, S. Li, et al., npj Quantum Mater. **4**, 12 (2019).

[12] K. Kitagawa, T. Takayama, Y. Matsumoto, et al., Nature **554**, 341 (2018).

[13] X. Liu, T. Berlijn, W.-G. Yin, W. Ku, A. Tsvelik, Y.-J. Kim, H. Gretarsson, Y. Singh, P. Gegenwart, and J. P. Hill, Phys. Rev. B **83**, 220403 (2011), URL `https://link.aps.org/doi/10.1103/PhysRevB.83.220403`.

[14] R. D. Johnson, S. C. Williams, A. A. Haghighirad, J. Singleton, V. Zapf, P. Manuel, I. I. Mazin, Y. Li, H. O. Jeschke, R. Valentí, et al., Phys. Rev. B **92**, 235119 (2015), URL `https://link.aps.org/doi/10.1103/PhysRevB.92.235119`.

[15] S. C. Williams, R. D. Johnson, F. Freund, S. Choi, A. Jesche, I. Kimchi, S. Manni, A. Bombardi, P. Manuel, P. Gegenwart, et al., Phys. Rev. B **93**, 195158 (2016), URL `https://link.aps.org/doi/10.1103/PhysRevB.93.195158`.

[16] A. Banerjee, P. Lampen-Kelley, J. Knolle, C. Balz, A. A. Aczel, B. Winn, Y. Liu, D. Pajerowski, J. Yan, C. A. Bridges, et al., npj Quantum Materials **3** (2018), URL `https://doi.org/10.1038%2Fs41535-018-0079-2`.

[17] H. Takagi, T. Takayama, G. Jackeli, et al., Nat Rev Phys **1**, 264 (2019).

[18] J. G. Rau, E. K.-H. Lee, and H.-Y. Kee, Phys. Rev. Lett. **112**, 077204 (2014), URL `https://link.aps.org/doi/10.1103/PhysRevLett.112.077204`.

[19] S. Choi, S. Manni, J. Singleton, C. V. Topping, T. Lancaster, S. J. Blundell, D. T. Adroja, V. Zapf, P. Gegenwart, and R. Coldea, Phys. Rev. B **99**, 054426 (2019), URL `https://link.aps.org/doi/10.1103/PhysRevB.99.054426`.

[20] K. Foyevtsova, H. O. Jeschke, I. I. Mazin, D. I. Khomskii, and R. Valentí, Phys. Rev. B **88**, 035107 (2013), URL `https://link.aps.org/doi/10.1103/PhysRevB.88.035107`.

[21] H. Gretarsson, J. P. Clancy, Y. Singh, P. Gegenwart, J. P. Hill, J. Kim, M. H. Upton, A. H. Said, D. Casa, T. Gog, et al., Phys. Rev. B **87**, 220407 (2013), URL `https://link.aps.org/doi/10.1103/PhysRevB.87.220407`.

[22] S. K. Choi, R. Coldea, A. N. Kolmogorov, T. Lancaster, I. I. Mazin, S. J. Blundell, P. G. Radaelli, Y. Singh, P. Gegenwart, K. R. Choi, et al., Phys. Rev. Lett. **108**, 127204 (2012), URL `https://link.aps.org/doi/10.1103/PhysRevLett.108.127204`.

[23] I. Kimchi and A. Vishwanath, Phys. Rev. B **89**, 014414 (2014), URL `https://link.aps.org/doi/10.1103/PhysRevB.89.014414`.

[24] P. Bhattacharyya, N. A. Bogdanov, S. Nishimoto, et al., npj Quantum Mater. **8**, 52 (2023).

[25] A. A. Aczel, A. M. Cook, T. J. Williams, S. Calder, A. D. Christianson, G.-X. Cao, D. Mandrus, Y.-B. Kim, and A. Paramekanti, Phys. Rev. B **93**, 214426 (2016), URL `https://link.aps.org/doi/10.1103/PhysRevB.93.214426`.

[26] E. S. Sørensen, A. Catuneanu, J. S. Gordon, and H.-Y. Kee, Phys. Rev. X **11**, 011013 (2021), URL `https://link.aps.org/doi/10.1103/PhysRevX.11.011013`.

[27] E. S. Sørensen, J. Gordon, J. Riddell, T. Wang, and H.-Y. Kee, Phys. Rev. Res. **5**, L012027 (2023), URL `https://link.aps.org/doi/10.1103/PhysRevResearch.5.L012027`.

[28] W. Yang, A. Nocera, and I. Affleck, Phys. Rev. Res. **2**, 033268 (2020), URL `https://link.aps.org/doi/10.1103/PhysRevResearch.2.033268`.

[29] C. M. Morris, N. Desai, J. Viirok, D. Hüvonen, U. Nagel, T. Rõõm, J. W. Krizan, R. J. Cava, T. M. McQueen, S. M. Koohpayeh, et al., Nat. Phys. **17**, 832 (2021).

[30] J. Rodriguez-Carvajal, **127** (1990).

[31] Bruker AXS Inc., *APEX4, SAINT, and SADABS*, Bruker AXS Inc., Madison, Wisconsin, USA (2021).

[32] O. V. Dolomanov, L. J. Bourhis, R. J. Gildea, J. A. K. Howard, and H. Puschmann, Journal of Applied Crystallography **42**, 339 (2009), URL `https://doi.org/10.1107/S0021889808042726`.

[33] G. M. Sheldrick, Acta Crystallographica Section A **71**, 3 (2015), URL `https://doi.org/10.1107/S2053273314026370`.

[34] G. M. Sheldrick, Acta Crystallographica Section C **71**, 3 (2015), URL `https://doi.org/10.1107/S2053229614024218`.

[35] B. T. Thole and G. van der Laan, Phys. Rev. A **38**, 1943 (1988), URL `https://link.aps.org/doi/10.1103/PhysRevA.38.1943`.

[36] D. Babel, W. Rüdorff, and R. Tschöpp, Zeitschrift für anorganische und allgemeine Chemie **347**, 282 (1966), `https://onlinelibrary.wiley.com/doi/pdf/10.1002/zaac.19663470509`, URL `https://onlinelibrary.wiley.com/doi/abs/10.1002/zaac.19663470509`.

[37] R. F. Sarkozy, C. W. Moeller, and B. Chamberland, Journal of Solid State Chemistry **9**, 242 (1974), ISSN 0022-4596, URL `https://www.sciencedirect.com/science/article/pii/0022459674900802`.

[38] F. Dijksma, J. Vente, E. Frikkee, and D. IJdo, Materials Research Bulletin **28**, 1145 (1993), ISSN 0025-5408, URL `https://www.sciencedirect.com/science/article/pii/002554089390094T`.

[39] M. Wakeshima, N. Taira, Y. Hinatsu, and Y. Ishii, Solid State Communications **125**, 311 (2003), ISSN 0038-1098, URL `https://www.sciencedirect.com/science/article/pii/S0038109802008232`.

[40] G. Cao, V. Durairaj, S. Chikara, S. Parkin, and P. Schlottmann, Phys. Rev. B **75**, 134402 (2007), URL `https://link.aps.org/doi/10.1103/PhysRevB.75.134402`.

[41] H. Hanate, T. Hasegawa, S. Hayami, S. Tsutsui, S. Kawano, and K. Matsuhira, Journal of the Physical Society of Japan **90**, 063702 (2021), URL `https://doi.org/10.7566/JPSJ.90.063702`.

[42] K. Akiba, T. C. Kobayashi, M. Hayashida, and K. Matsuhira, Journal of the Physical Society of Japan **92**, 035002 (2023), URL `https://doi.org/10.7566/JPSJ.92.035002`.

[43] H. Müller-Buschbaum, Journal of Alloys and Compounds **349**, 49 (2003), ISSN 0925-8388, URL `https://www.sciencedirect.com/science/article/pii/S0925838802009258`.

[44] N. Keawprak, R. Tu, and T. Goto, MATERIALS TRANSACTIONS **50**, 853 (2009).

[45] V. Singh and J. Pulikkotil, Computational Materials Science **153**, 97 (2018), ISSN 0927-0256, URL `https://www.sciencedirect.com/science/article/pii/S0927025618303240`.

[46] Kraus, W. and Nolze, G., *PowderCell for Windows, Version 2.4*, Federal Institute for Materials Research and Testing, Berlin, Germany (2000).

[47] C. McDaniel and S. Schneider, Journal of Solid State Chemistry **4**, 275 (1972), ISSN 0022-4596, URL `https://www.sciencedirect.com/science/article/pii/002245967290117X`.

[48] X. Chen and S. D. Wilson, Phys. Rev. B **94**, 195115 (2016), URL `https://link.aps.org/doi/10.1103/PhysRevB.94.195115`.

[49] S. Haneta, Y. Yasukuni, C. Oka, M. Wakeshima, Y. Hinatsu, and K. Matsuhira, Journal of Magnetism and Magnetic Materials **476**, 274 (2019), ISSN 0304-8853, URL `https://www.sciencedirect.com/science/article/pii/S0304885318324867`.

[50] e. a. Robin, *Database of Ionic Radii*, Atomistic Simulation Group - Department of Materials - Imperial College London (1976), URL `http://abulafia.mt.ic.ac.uk/shannon/ptable.php`.

[51] S. M. Disseler, C. Dhital, A. Amato, S. R. Giblin, C. de la Cruz, S. D. Wilson, and M. J. Graf, Phys. Rev. B **86**, 014428 (2012), URL `https://link.aps.org/doi/10.1103/PhysRevB.86.014428`.